AGU ADVANCING EARTH AND SPACE SCIENCES

Space Weather

RESEARCH ARTICLE
10.1029/2025SW004353

Key Points:

- Field-aligned current (FAC) during high-intensity long-duration continuous auroral electrojet activity (HILDCAA) is ~5 times the quiet-FAC intensity
- HILDCAA-related FAC variation is characterized by periodicities of ~11 and ~19 hr, well correlated to the SML variations
- The average FAC response time to the interplanetary magnetic field B_z is ~28 ± 17 min during the HILDCAAs

Correspondence to:
R. Hajra,
rhajra@ustc.edu.cn;
rajkumarhajra@yahoo.co.in

Citation:
Hajra, R., Tsurutani, B. T., Lu, Q., Du, A., Lu, S., & Gao, X. (2025). Field-aligned currents during high-intensity long-duration continuous auroral electrojet activity events: A statistical study. *Space Weather*, *23*, e2025SW004353. https://doi.org/10.1029/2025SW004353

Received 15 JAN 2025
Accepted 24 SEP 2025

Author Contributions:
Conceptualization: Rajkumar Hajra, Bruce T. Tsurutani
Data curation: Rajkumar Hajra
Formal analysis: Rajkumar Hajra
Investigation: Rajkumar Hajra
Methodology: Rajkumar Hajra
Resources: Rajkumar Hajra
Supervision: Rajkumar Hajra, Bruce T. Tsurutani
Validation: Rajkumar Hajra
Visualization: Rajkumar Hajra
Writing – original draft: Rajkumar Hajra
Writing – review & editing: Rajkumar Hajra, Bruce T. Tsurutani, Quanming Lu, Aimin Du, San Lu, Xinliang Gao

Field-Aligned Currents During High-Intensity Long-Duration Continuous Auroral Electrojet Activity Events: A Statistical Study

Rajkumar Hajra[1], Bruce T. Tsurutani[3], Quanming Lu[1], Aimin Du[2], San Lu[1], and Xinliang Gao[1]

[1]CAS Key Laboratory of Geospace Environment, School of Earth and Space Sciences, University of Science and Technology of China, Hefei, China, [2]College of Earth and Planetary Sciences, Chinese Academy of Sciences, Beijing, China, [3]Retired, Pasadena, CA, USA

Abstract Enhanced solar wind-magnetosphere energy coupling during geomagnetic disturbances leads to strong geomagnetic field-aligned currents (FACs). While variations of FACs during geomagnetic storms and substorms have been well explored, there is no systematic study of FACs during high-intensity long-duration continuous auroral electrojet activities (HILDCAAs). Substorm studies usually involve the quiet solar wind and storm studies typically involve interplanetary coronal mass ejections and their sheaths, while HILDCAAs typically involve high-speed streams. Here we present, for the first time, a statistical study of HILDCAA-related FAC variation based on measurements by the Active Magnetosphere and Planetary Electrodynamics Response Experiment from 2009 through 2023. During HILDCAAs, FACs are found to extend in a large region, from the pole down to ~65° magnetic latitude, with a characteristic peak intensity ~5 times the quiet time FAC intensity. The FAC intensity variation is characterized by periodicities of ~19 and ~11 hr (in descending order of spectral power), well correlated to the auroral electrojet current westward component SML. On average, the HILDCAA-related FAC variation is delayed from the Alfvén wave interplanetary magnetic field B_z component fluctuations by ~28 ± 17 min. The HILDCAA onset is marked by a sharp increase in average FAC intensity temporal profile, peaking ~14 hr after the HILDCAA onset time. The HILDCAA-related FAC intensification is found to be associated with enhanced magnetic flux opening and energy transfer at the dayside magnetopause. The results are consistent with FAC relationships with solar wind variations and geomagnetic conditions reported previously for geomagnetic storms and substorms.

Plain Language Summary Energy flow from the solar wind into the Earth's magnetosphere-ionosphere system leads to strong geomagnetic field-aligned currents (FACs). High-intensity long-duration continuous auroral electrojet activity (HILDCAA) events are associated with strong convection events continuing for several days to weeks, conducive of strong FAC generation. However, HILDCAA-related FAC variations are not well understood. Based on a long-term database of FAC measurements, we identified strong FACs extending from the pole down to ~65° magnetic latitude during HILDCAAs. Short-term fluctuations in FACs are found to be correlated to the typical auroral electrojet variations during HILDCAAs, caused by interplanetary Alfvén waves. From statistical analyses, we identified an association of HILDCAA-related FACs with enhanced magnetic flux opening and energy transfer at the dayside magnetopause.

1. Introduction

Interplanetary Alfvén waves (Alfvén, 1942; Belcher & Davis, 1971) carried by solar wind high-speed (~550–850 km s^{-1}) streams (HSSs; Neugebauer & Snyder, 1966; Phillips et al., 1995; Tsurutani et al., 2006) emanated from solar coronal holes (Krieger et al., 1973) cause high-intensity long-duration continuous auroral electrojet (AE) activity (HILDCAA) events (Hajra et al., 2013; Tsurutani & Gonzalez, 1987). Magnetic reconnection (Dungey, 1961) between the Alfvén wave southward components and (northward) geomagnetic fields at the Earth's dayside magnetopause leads to substorm/convection events during HILDCAAs. Viscous interaction (Axford & Hines, 1961) also transfers solar wind energy to the magnetosphere. The substorm/convection events, in turn, lead to enhancements of the auroral region Birkeland currents flowing parallel to the geomagnetic fields, commonly known as the field-aligned currents (FACs). FACs were first proposed theoretically by Birkeland (1908, 1913), followed by their space-based identification by the polar orbiting satellite 1962 38C (Zmuda et al., 1966). The currents electrodynamically couple the magnetopause, the inner magnetosphere, and the ionosphere. They consist of two components (Clausen et al., 2012; Cowley, 2000; Iijima & Potemra, 1976, 1978). The poleward component, known as the region 1 current, flows through the ionosphere extending from the dayside magnetopause to the magnetotail. The equatorward region 2 current component flows through the partial ring current in the inner magnetosphere. Both of these two components are reported to increase significantly during the substorm expansion phase (e.g., Coxon et al., 2014; Forsyth et al., 2018; Iijima & Potemra, 1978; Käki et al., 2022). Geomagnetic storms cause FAC enhancements, maximizing during the storm main phase (Hajra, Tsurutani, Lakhina, et al., 2024; Hajra, Tsurutani, Lu, Horne, et al., 2024; Knipp et al., 2014; Le et al., 2016; Lyons et al., 2016; Pedersen et al., 2021, 2022; Wilder et al., 2012). While FAC (quiet time) statistical features (e.g., Cheng et al., 2018; Coxon et al., 2016; Fujii et al., 1981; Hajra et al., 2025; Laundal et al., 2018; Qu et al., 2024; Wang & Lühr, 2023; Wang et al., 2024), their variations during geomagnetic storms and substorms (see references above) have been studied previously, there are no studies on FACs during HILDCAAs. Solar wind/interplanetary conditions and magnetospheric convection are significantly different for HILDCAAs than those for storms and substorms. HILDCAAs represent long intervals of very strong and high-frequency auroral activities (Guarnieri et al., 2018; Kozyra et al., 2006; Mendes et al., 2017; Souza et al., 2016, 2018; Tsurutani et al., 1995; Turner et al., 2006) leading to enhanced magnetospheric convection continuing for days to weeks (Hajra et al., 2014b; Sandanger et al., 2005; Søraas et al., 2004; Tsurutani et al., 2004, 2006). Thus, complex FAC variability can be expected to occur during the HILDCAAs.

In this paper, we analyze the FAC variations during a large number of HILDCAA events. Solar wind plasma, interplanetary and geomagnetic activity measurements are used in the analyses. The major questions explored in this work are as follows. How intense are FACs during HILDCAAs? Is the FAC variability correlated to auroral activity and causally connected to the interplanetary variations?

2. Data and Methods

Period of study: The focus of this study is the variations of FACs during HILDCAAs, using FACs measured by the Active Magnetosphere and Planetary Electrodynamics Response Experiment (AMPERE; Anderson et al., 2000, 2002, 2021; Waters et al., 2001, 2020). We thus chose the period when AMPERE FAC measurements are available, that is, from October 2009 through December 2023. There is a measurement gap from May 2018 to February 2019.

Data sources: We obtained FAC data from the AMPERE Science Data Center of the Johns Hopkins Applied Physics Laboratory that provides FAC measurements in the northern and southern hemispheres above 40° magnetic latitude (MLAT). The FAC estimations are based on the magnetic perturbations measured by 66 satellites of the Iridium telecommunication network in six polar orbital planes at an altitude of ∼780 km (orbital period of ∼104 min). For the present analyses, we use (a) the northern and southern hemispheric FAC density maps in altitude-adjusted corrected geomagnetic (AACGM) latitude (Baker & Wing, 1989) and magnetic local time (MLT) coordinate system, averaged over 10 min; and (b) temporal variations (2-min resolution) of integrated FAC intensities (Anderson et al., 2014, 2021) separated into upward and downward, dayside and nightside components in northern and southern hemispheres. It is worth mentioning that continued measurements and large space coverage by large numbers of satellites make AMPERE more useful than other spatially sparse satellite observations in studying large-scale structures and temporal evolutions of FACs. However, use of 10-min sliding windows every 2 min to measure FACs implies lower temporal resolution. This is not a problem for the present large-scale study.

The near-Earth solar wind plasma and interplanetary magnetic field (IMF) data (1-min resolution) are obtained from NASA's OMNIWeb Plus database (King & Papitashvili, 2020). These are based on measurements by multiple upstream spacecraft, such as, Advanced Composition Explorer (ACE), Wind, Interplanetary Monitoring Platform (IMP) 8 and Geotail. The in situ measurements are shifted (in time) to the Earth's bow shock nose for a direct comparison with inner magnetospheric/geomagnetic variations. The IMF vector components are in the geocentric solar magnetospheric (GSM) coordinate system. This system has the x-axis directed toward the sun, and the y-axis is in the $\mathbf{\Omega} \times \hat{\mathbf{x}}/|\mathbf{\Omega} \times \hat{\mathbf{x}}|$-direction, where $\mathbf{\Omega}$ is the direction of the magnetic south-pole of the Earth. The z-axis completes a right-hand system.

The solar coronal images at 193 Å are obtained from the Atmospheric Imaging Assembly (AIA) instrument onboard NASA's Solar Dynamics Observatory (SDO). Solar synoptic maps are obtained from the Space Weather Prediction Center of the National Oceanic and Atmospheric Administration (NOAA).

The geomagnetic Dst (1-hr), AE (1-min), and SYM-H (1-min) indices are obtained from the World Data Center for Geomagnetism, Kyoto, Japan. The auroral electrojet indices (1-min) SME, and SML are obtained from the SuperMAG database (Gjerloev, 2009, 2012; Newell & Gjerloev, 2011a, 2011b). The yearly mean $F_{10.7}$ solar fluxes are obtained from the Laboratory for Atmospheric and Space Physics Interactive Solar Irradiance Data Center.

HILDCAA identification: HILDCAAs are identified based on original criteria suggested by Tsurutani and Gonzalez (1987): (a) the peak AE intensity ≥ 1,000 nT, (b) the event duration ≥ 2 days, (c) AE never drops below 200 nT for more than 2 hr at a time, and (d) the event occurs outside the main phase of geomagnetic storms. Accordingly, we searched for the SME > 1,000 nT events from the SME time series (we used SME instead of AE, see below). The data were then scanned both forward and backward in time to verify that SME did not decrease below 200 nT for more than 2 hr at a time. If the event was longer than 2 days, and if SYM-H was >−50 nT, this was categorized as a HILDCAA event (SYM-H is used instead of Dst). Thus, by definition, the HILDCAA onset (end) time is the first (last) time SME becomes greater than 200 nT. Forty-eight HILDCAAs were identified during 2009 through 2023, which are listed in Table 1. Only 42 HILDCAAs had suitable FAC measurements available.

As AE is derived based on observations from 12 geomagnetic stations (∼60°N–70°N; Ahn et al., 2000; Kamide & Akasofu, 1983; Rostoker, 1972), it may be insufficient for auroral activities occurring at very low latitudes (e.g., during intense geomagnetic activity) or at very high latitudes (for weak geomagnetic activity intervals). On the other hand, the SME index is based on ∼300 ground magnetometer observations (∼40°N–80°N) under the SuperMAG network, including the standard AE magnetometer sites. Thus, SME can identify auroral activity in a wide region from mid-latitudes to high-latitudes. We also used high-resolution (1-min) SYM-H index instead of low-resolution (1-hr) Dst index to quantify geomagnetic conditions. Use of the SME and SYM-H indices resulted in a significant increase in the HILDCAA number: from October 2009 through December 2019 (note that AE data is not available after 2019), the number of HILDCAAs using the AE and Dst indices is 17, while the HILDCAA number using the SME and SYM-H indices during the same interval is 43, giving a much bigger database.

Each of the HILDCAAs is characterized by a peak SME intensity (SMEp), and duration of the event. Figure 1 shows distributions of yearly numbers of HILDCAAs (Figure 1a), characteristic SMEp (Figure 1b), and duration of the events (Figure 1c). While HILDCAAs are observed during all phases of the solar cycle (the solar cycle phases can be seen from the yearly mean $F_{10.7}$ solar flux variation), ∼56% of the HILDCAAs are identified during the solar cycle descending-to-minimum phase between 2014 and 2019. The highest yearly number of HILDCAAs is 10, recorded during 2017. The HILDCAA SMEp varies between 1,017 and 2,162 nT, with an average (median) intensity of ∼1,388 ± 256 (∼1,383) nT for all HILDCAAs (the number following ± symbol indicates 1-σ deviation). No supersubstorms with the SML peak intensity ≤−2,500 nT (Hajra & Tsurutani, 2018; Hajra et al., 2016; Hajra, Echer, et al., 2023; Tsurutani & Hajra, 2023; Tsurutani et al., 2015) were identified in this study. The shortest and longest HILDCAA durations recorded in this study are 2.00 days (by selection criteria/definition) and 6.30 days, respectively, with a mean (median) duration of ∼2.90 ± 0.92 (∼2.61) days for all events.

Interplanetary CIR and HSS identifications: Near-Earth solar wind plasma and IMF variations are analyzed to identify HSSs and interplanetary corotating interaction regions (CIRs). A fast rise in the solar wind proton speed V_p to a maximum of ∼550–850 km s^{-1}, followed by a slower decay characterize a typical HSS at 1 au (Tsurutani et al., 1995, 2005). Identification of an HSS is then confirmed by identification of a coronal hole at the sun (Krieger et al., 1973) ∼2–3 days prior to the near-Earth V_p peak occurrence (considering propagation time of a V_p ∼550–850 km s^{-1} stream from the sun to Earth). The proton temperature T_p more or less follows the HSS V_p temporal profile. In the interaction region between a slow stream and an HSS, a gradual increase in V_p is accompanied by enhancements in proton density N_p, ram pressure P_{sw}, and IMF magnitude B_0. This compressed plasma and IMF region is identified as a CIR (Smith & Wolfe, 1976). The IMF components B_x, B_y, and B_z exhibit fluctuations in their amplitudes and polarities (indicative of interplanetary Alfvén waves; Belcher & Davis, 1971; Coleman, 1966; Neugebauer et al., 1984) during an HSS, which are significantly amplified during the CIR.

Interplanetary discontinuities: Several types of interplanetary discontinuities are identified in and around a CIR. A stream interface (SI) separates the compressed slow solar wind part of a CIR at its antisolar side from its compressed HSS part at the solar side (Belcher & Davis, 1971; Burlaga, 1974; Hundhausen & Burlaga, 1975). It is identified by (a) an abrupt decrease in N_p, (b) a simultaneous increase in T_p, (c) a small increase in V_p, following Burlaga (1974), and by (d) an alpha density-to-N_p ratio increase, as suggested by Gosling et al. (1978). Some of the CIRs are bounded by a fast forward (FF) shock at its leading edge and a fast reverse (FR) shock at the trailing edge. An FF (FR) shock is identified from a sharp increase in V_p accompanied by simultaneous and sharp

Table 1
HILDCAAs Identified During 2009–2023

Start (Date UT)	End (Date UT)	Duration (days)	SME peak (nT)	SYM-H peak (nT)
24 August 2010 09:41	26 August 2010 16:46	2.30	1,228	−40
01 April 2011 08:23	04 April 2011 08:09	2.99	1,322	−45
07 June 2011 11:03	09 June 2011 23:42	2.53	1,017	−47
13 June 2011 09:40	15 June 2011 23:18	2.57	1,119	−16
22 June 2011 08:52	24 Junee 2011 22:15	2.56	1,021	−35
08 July 2011 06:44	10 July 2011 09:34	2.12	1,067	−39
19 July 2011 05:08	21 July 2011 07:13	2.09	1,122	−26
21 July 2011 11:46	23 July 2011 12:14	2.02	1,219	−26
11 September 2011 12:17	13 September 2011 13:05	2.03	1,390	−50
04 June 2012 02:11	07 June 2012 10:27	3.34	1,438	−32
29 June 2012 19:27	03 July 2012 18:27	3.96	1,332	−35
26 May 2013 12:40	28 May 2013 15:36	2.12	1,123	−40
19 June 2013 14:28	25 June 2013 21:47	6.30	1,397	−44
25 July 2013 15:08	28 July 2013 16:58	3.08	1,141	−25
21 August 2013 02:51	24 August 2013 01:21	2.94	1,131	−46
01 January 2014 00:39	03 January 2014 00:40	2.00	1,392	−39
23 September 2014 06:41	27 September 2014 20:32	4.58	1,329	−34
06 December 2014 18:32	10 December 2014 02:59	3.35	1,589	−34
20 April 2015 17:57	22 April 2015 18:55	2.04	1,439	−35
12 June 2015 10:04	16 June 2015 20:12	4.42	1,903	−36
15 September 2015 07:57	17 September 2015 12:36	2.19	1,223	−36
01 October 2015 06:16	03 October 2015 20:25	2.59	1,146	−35
10 December 2015 00:11	12 December 2015 22:43	2.94	1,611	−19
11 July 2016 10:23	13 July 2016 15:23	2.21	1,437	−44
16 October 2016 06:04	18 October 2016 16:40	2.44	1,459	−34
09 December 2016 05:40	11 December 2016 20:44	2.63	1,583	−48
05 January 2017 12:07	09 January 2017 19:12	4.30	1,478	−47
31 January 2017 14:11	04 February 2017 01:31	3.47	1,692	−48
04 February 2017 04:43	06 February 2017 05:06	2.02	1,350	−31
03 March 2017 23:57	06 March 2017 04:05	2.17	1,268	−44
21 March 2017 04:22	23 March 2017 10:37	2.26	1,490	−46
19 May 2017 12:57	21 May 2017 13:30	2.02	1,311	−44
24 July 2017 03:27	26 July 2017 18:33	2.63	1,356	−26
04 August 2017 05:29	06 August 2017 14:02	2.36	1,573	−35
17 August 2017 03:40	21 August 2017 12:50	4.38	2162	−46
14 September 2017 11:19	17 September 2017 20:40	3.39	1,854	−44
24 October 2017 08:49	26 October 2017 20:03	2.47	1,912	−44
08 May 2018 14:37 [a]	11 May 2018 10:54	2.85	1,032	−35
31 May 2018 14:39 [a]	03 June 2018 22:47	3.34	1,375	−49
21 September 2018 20:22 [a]	24 September 2018 03:19	2.29	1,522	−49
08 October 2018 23:47 [a]	11 October 2018 21:51	2.92	1,626	−49
31 January 2019 09:40 [a]	03 February 2019 22:56	3.55	1,554	−39
27 February 2019 12:07 [a]	03 March 2019 19:14	4.30	1,547	−45

Table 1
Continued

Start (Date UT)	End (Date UT)	Duration (days)	SME peak (nT)	SYM-H peak (nT)
15 June 2021 10:53	17 June 2021 12:03	2.05	1,020	−33
11 February 2022 18:56	14 February 2022 18:49	3.00	1,150	−46
27 April 2022 12:45	30 April 2022 11:41	2.96	1,614	−46
02 March 2023 17:13	07 March 2023 00:00	4.28	1,430	−45
30 March 2023 00:55	01 April 2023 00:56	2.00	1,142	−39

[a]No FAC measurements are available during HILDCAAs occurring during 2018–2019.

increases (decreases) in N_p, P_{sw}, T_p, and IMF B_0. Identification of an FF/FR shock is confirmed by estimated magnetosonic Mach number $M_{ms} > 1$. Discontinuities with $M_{ms} < 1$ are classified as steepened waves. Detail methods of determining the discontinuity characteristic parameters, using the Abraham-Shrauner (1972) mixed-mode method and the Rankine–Hugoniot (Hugoniot, 1887, 1889; Rankine, 1870) conservation laws, can be found in literature (e.g., Hajra, 2021a; Hajra & Tsurutani, 2018; Hajra, Tsurutani, et al., 2023; Hajra et al., 2016, 2018, 2020; Smith, 1985; Tsurutani & Lin, 1985; Tsurutani et al., 2011).

Solar wind-magnetosphere coupling: Solar wind-magnetosphere coupling during the HILDCAA events is quantified using several coupling functions. An important driver of geomagnetic activity is the interplanetary motional (eastward) electric field VB_s (Burton et al., 1975; Finch et al., 2008; Tsurutani et al., 1992), where V is the solar wind V_p, and B_s is the southward component of IMF. An empirical estimate of magnetospheric energy input rate is given by the ε-parameter: $V_p B_0^2 \sin^4(\theta/2) R_{CF}^2$ (Perreault & Akasofu, 1978), where θ is the IMF clock angle, R_{CF} is the magnetopause scale size, $R_{CF} = \left(2B_E^2/\left(\mu_0 m_p N_p V_p^2\right)\right)^{1/6} R_E$ (Chapman & Ferraro, 1931), B_E is the equatorial magnetic field on the Earth's surface, μ_0 is the free space permeability, m_p is the proton mass, and R_E is the Earth's radius. The dayside reconnection rate or the magnetic flux transport across the dayside magnetosphere

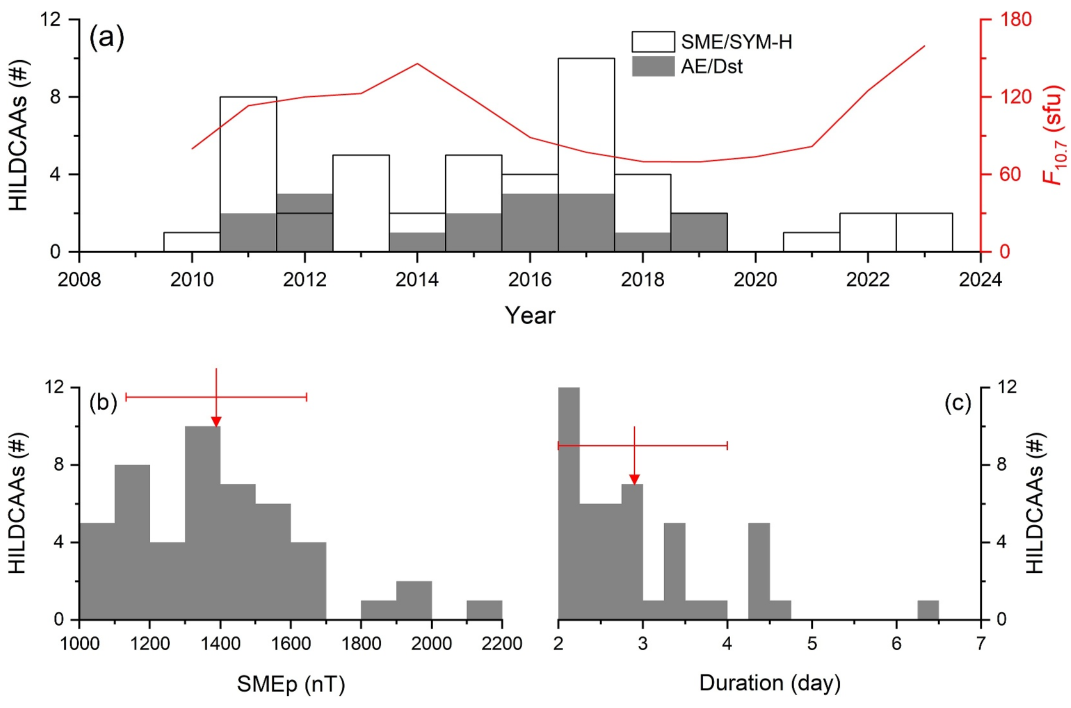

Figure 1. (a) Yearly numbers of HILDCAAs (histograms, legend on the left) and the yearly mean $F_{10.7}$ solar flux variation (red lines, legend on the right), $F_{10.7}$ is given in solar flux unit (sfu), 1 sfu = 10^{-22} W m^{-2} Hz^{-1}. HILDCAAs identified by using the SME and SYM-H indices (2009–2023) are shown by empty histograms, while those by AE and Dst (2009–2019) are shown by light-gray histograms. Distributions of (b) the peak SME (SMEp) during HILDCAAs, and (c) the HILDCAA duration. The mean values and 1-σ deviations are shown by downward arrows and horizontal bars, respectively.

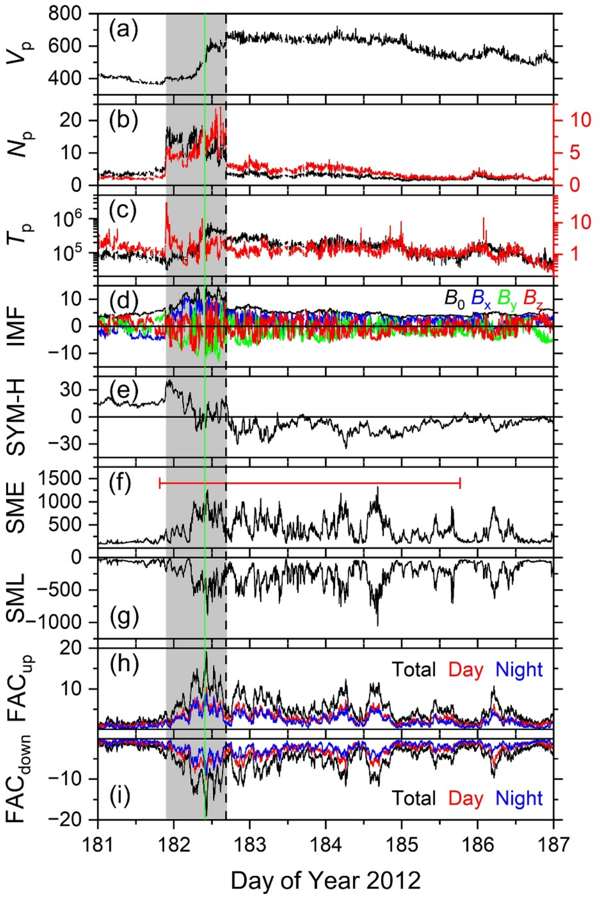

Figure 2. A HILDCAA and associated FACs during days 181–186 (29 June–3 July) of 2012. From top to bottom, panels are: (a) solar wind proton speed V_p (km s^{-1}), (b) proton density N_p (cm^{-3}, black, legend on the left) and ram pressure P_{sw} (nPa, red, legend on the right), (c) proton temperature T_p (K, black, legend on the left) and plasma-β (red, legend on the right), (d) interplanetary magnetic field (IMF) magnitude B_0 (nT, black), and B_x (nT, blue), B_y (nT, green), and B_z (nT, red) components, (e) symmetric ring current index SYM-H (nT), (f) auroral electrojet index SME (nT), (g) auroral electrojet westward component SML (nT), and total northern and southern hemispheric integrated (h) upward FAC intensity FAC_{up} (MA), and (i) downward FAC intensity FAC_{down} (MA). Vertical gray shading indicates a corotating interaction region (CIR), with a fast reverse (FR) shock shown by a vertical dashed line at the CIR trailing edge. The green vertical solid line marks occurrence of a stream interface (SI). The red horizontal bar in the SME panel (f) indicates the HILDCAA interval.

is estimated as: $\Phi_D = 3.2 \times 10^5 V_p^{4/3} B_{yz} \sin^{9/2}(\theta/2)$ (Milan et al., 2012), where $B_{yz} = \left(B_y^2 + B_z^2\right)^{1/2}$. The Newell coupling function N_{CF}, a measure of the rate of open magnetic flux Φ_{MP} generation at the magnetopause, is given by: $d\Phi_{MP}/dt = V_p^{4/3} B_{yz}^{2/3} \sin^{8/3}(\theta/2)$ (Newell et al., 2007).

Superposed epoch analyses: Superposed epoch analyses were conducted to identify the average features of the HILDCAA-related geomagnetic activity, currents and causative solar and interplanetary parameters. The HILDCAA onset time is taken as the zero epoch time. We considered intervals from 2 days before to 5 days after the HILDCAA onset for the analyses.

Wavelet analyses: We performed wavelet transform analyses (Torrence & Compo, 1998) of SML and FACs to study their periodic variations during HILDCAAs. The periodograms are developed using continuous Morlet wavelet function. Significant periods of SML and FAC variations are identified from high powers in the periodograms. The cone of influence is introduced to indicate edge artifacts (potentially distorting the results) in the wavelets. Further details can be found in Souza et al. (2016, 2018), and Hajra et al. (2021).

Cross-correlation analyses: We performed time-lagged cross-correlation analyses (Davis, 2002) between IMF B_z and SML, B_z and FAC, and FAC and SML. The 1-min resolution B_z and SML data are processed into 2 min (by taking 2-min running averages) so that they precisely coincide (in time) with the FAC data (2-min resolution) to avoid any artificial time lag.

Statistical probability factor: Significance of the statistical results presented in this work is verified by computation of two-tailed p-values (Reiff, 1990). Considering that the parameters may not have normal distributions, nonparametric Wilcoxon Rank Sum test (Gibbons & Chakraborti, 2011) is used for the p-value computation using the median values of the parameters and number of events. A p-value less than 0.05 suggests that the two medians are significantly (statistically) different from each other (Press et al., 1992).

3. Results

3.1. Case Study of FACs Associated With a HILDCAA Occurring on Days 181–185 (29 June–3 July) of 2012

Figure 2 shows solar wind plasma and IMF variations along with geomagnetic indices and FAC measurements during a HILDCAA event occurring on days 181–185 (29 June–3 July) of 2012. The ~3.96 days-long HILDCAA, from 19:27 UT on day 181 to 18:27 UT on day 185 (marked by a horizontal bar in the SME panel), is characterized by strong SME (peak 1,332 nT, Figure 2f) and SML intensities (minimum −1,054 nT, Figure 2g), while the SYM-H minimum was only −35 nT (Figure 2e) indicating ring current activity weaker than the geomagnetic storm threshold (SYM-H ≤ −50 nT; Gonzalez et al., 1994).

This is a typical HILDCAA event associated with a CIR followed by an HSS proper, typical interplanetary solar wind features described in several previous works (e.g., Hajra, 2021b; Hajra et al., 2013, 2014a, 2014b, 2014c, 2015a, 2015b, 2020; Hajra, Tsurutani, Lu, Lakhina, et al., 2024; Tsurutani & Gonzalez, 1987; Tsurutani et al., 2006). Here we describe them briefly for the reader. From the temporal variation of solar wind V_p (Figure 2a), a slow solar wind stream with V_p of ~368–427 km s^{-1} is identified on day 181. An HSS is observed during days 182–185, having a peak V_p of ~725 km s^{-1}. The HSS was emanated from a large, equatorial coronal hole (marked by a NOAA number 21) with a negative magnetic polarity (i.e., magnetic field pointing toward the sun; see Appendix A Figure A1). This is consistent with the positive B_x- and negative B_y-components indicating a sunward IMF direction (Figure 2d).

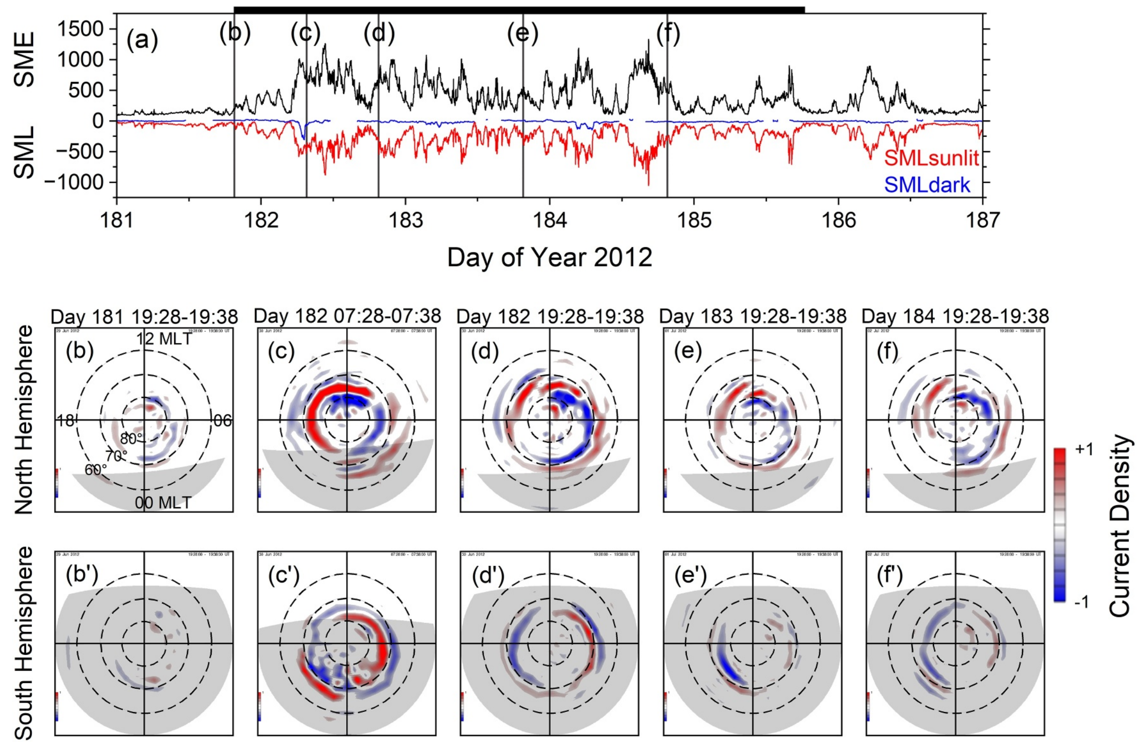

Figure 3. Hemispheric FAC density maps during the HILDCAA event shown in Figure 2. (a) Temporal variations of total SME index (nT, black), sunlit (red) and dark (blue) ionospheric SML indices (nT). The HILDCAA interval is marked by a horizontal bar at the top. (b–f, b′–f′) The average radial FAC density (μA m^{-2}) for the northern hemisphere (middle panels) and the southern hemisphere (bottom panels) plotted in the AACGM latitude and MLT coordinates for 10-min time intervals marked by vertical gray shadings and corresponding panel numbers in panel (a). The red and blue in the current density maps identify upward and downward current components, respectively.

The interaction region between the slow stream and the HSS is characterized by gradual increases in V_p (Figure 2a) and T_p (Figure 2c), and enhancements and fluctuations in N_p, P_{sw} (Figure 2b), and IMF B_0 (Figure 2d)—indicting compressions of solar wind plasma and IMF, known as a CIR (marked by a vertical gray shading). The CIR trailing edge is characterized by a sharp small increase in V_p (∼618–662 km s^{-1}), accompanied by sharp and simultaneous decreases in N_p (∼11.6–3.7 cm^{-3}), P_{sw} (∼9.0–3.3 nPa), T_p (∼47.9 × 10^4 to 25.0 × 10^4 K) and B_0 (∼9.7–6.3 nT) at ∼16:31 UT on day 182. The discontinuity is determined to be an FR shock, characterized by an M_{ms} of ∼1.77, a shock speed V_{sh} (relative to the upstream solar wind plasma speed) of ∼131 km s^{-1}, and a shock angle θ_{Bn} of ∼52° with respect to the upstream ambient IMF. An SI is identified at ∼14:48 UT on day 182, inside the CIR, characterized by a ∼16.2 to 8.2 cm^{-3} decrease in N_p, and a ∼30.0 × 10^4 to 52.0 × 10^4 K increase in T_p. The HSS carried Alfvén waves as indicated by fluctuating IMF components, the wave amplitude being amplified in the CIR.

FAC variations: Figures 2h and 2i show the upward and downward FAC intensity variations during the HILDCAA, respectively. These are the total currents, combining both the northern and southern hemispheric currents. While the HILDCAA event (occurring during 29 June through 3 July) corresponds to northern hemispheric summer and southern hemispheric winter, combining measurements in both hemispheres removes any seasonal dependence of FACs. The HILDCAA onset is marked by prominent increases in FAC intensities, and they seem to exhibit general association with the SME/SML variations during the HILDCAA. Upward (downward) total FAC intensity peaks (FACp) to ∼19.2 (−19.1) MA at ∼10:16 UT on day 182, ∼14.8 hr after the HILDCAA onset, with an average FAC intensity (<FAC>) of 6.0 ± 3.0 (−5.8 ± 2.8) MA during the entire HILDCAA interval. FACp and <FAC> are defined as the characteristic peak and average FAC intensities of the HILDCAA, respectively. Thus, the HILDCAA corresponds to enhanced FACs compared to the pre-HILDCAA FAC intensities of ∼0.7–3.3 MA. There is no significant difference between the dayside and nightside FAC intensities.

Figure 3a shows the SME index along with SML separated into sunlit and dark ionospheric SML values during the HILDCAA event shown in Figure 2. It should be noted that the SME and SML indices are based on northern hemispheric measurements. As the HILDCAA event corresponds to the northern hemispheric summer, when

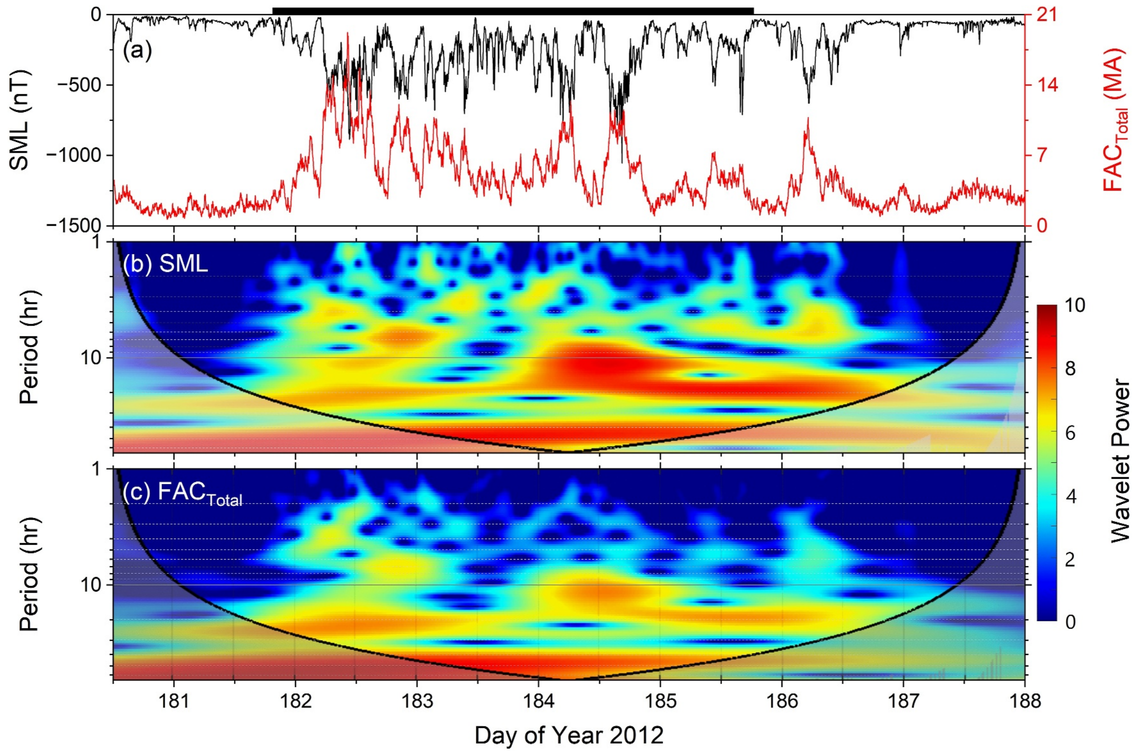

Figure 4. Wavelet analyses during the HILDCAA event shown in Figure 2. (a) Temporal variations of the SML index (black, legend on the left), and total upward FAC intensity (red, legend on the right). The HILDCAA interval is marked by a horizontal bar at the top. Wavelet spectrum periodograms of (b) the SML index, and (c) total upward FAC intensity. The cone of influence is shown by the black curve; and region outside this, where edge effects might distort the results, is marked by light shading. Rainbow color bar on the right shows the wavelet spectral power of the observed periods in arbitrary units.

major part (MLT sectors) of the high-latitude northern hemisphere is sunlit, the dark ionospheric SML is insignificant, and the sunlit values account for the total SML variation (shown in Figure 2g). The northern and southern hemispheric FAC maps are shown during different phases of the HILDCAA (Figures 3b–3f, 3b′–3f′). Polar ionospheric illumination variations between the two hemispheres are marked in the maps. Northern hemispheric FAC maps show that dark-region FACs are insignificant compared to sunlit-region FACs (Figures 3b–3f), consistent with the dark and sunlit ionospheric (northern hemispheric) SML variations (Figure 3a).

At the HILDCAA onset, all MLT sectors for AACGM latitude >70° are sunlit (dark) in the northern (southern) hemisphere (Figures 3b and 3b′). The FAC maps show only weak currents corresponding to pre-HILDCAA (quiet) geomagnetic conditions.

At 12 hr after the HILDCAA onset, both dark and sunlit region SML indices are enhanced (Figure 3a, second vertical shading). Corresponding FAC map in the northern hemisphere (Figure 3c) shows strong region 1 (70–85° latitude) upward current (red) in the 9–22 MLT sector, weaker downward current (blue) in the 0–8 MLT sector. Another strong downward current is observed in the 8–15 MLT sector at >78° latitude, extending up to the pole (region 0). These correspond to sunlit ionosphere. In the northern hemisphere, region 2 (65–70° latitude) upward (downward) current is observed around 23–6 MLT (12–21 MLT) sector. In the southern hemisphere (Figure 3c′), region 1 upward (downward) current is observed in the 3–12 MLT (12–23 MLT) sector. Region 2 upward (downward) current is observed in the 19–23 MLT (1–6 MLT) sector. Most of these correspond to dark ionosphere.

At 1 day after the HILDCAA onset, sunlit region SML is significantly enhanced while dark side SML is insignificant (Figure 3a, third vertical shading). This is consistent with stronger northern hemispheric (mostly sunlit) FACs (Figure 3d) than the southern hemispheric (entirely dark) FACs (Figure 3d′). In the northern hemisphere, near-pole region 0 upward current is observed in the 6–12 MLT. In region 1, upward current is observed in the 9–18 MLT sector, downward current is observed in the 0–12 MLT sector. In region 2, upward current is observed in the 21–9 MLT sector, downward current is observed in the 15–19 MLT sector. In the

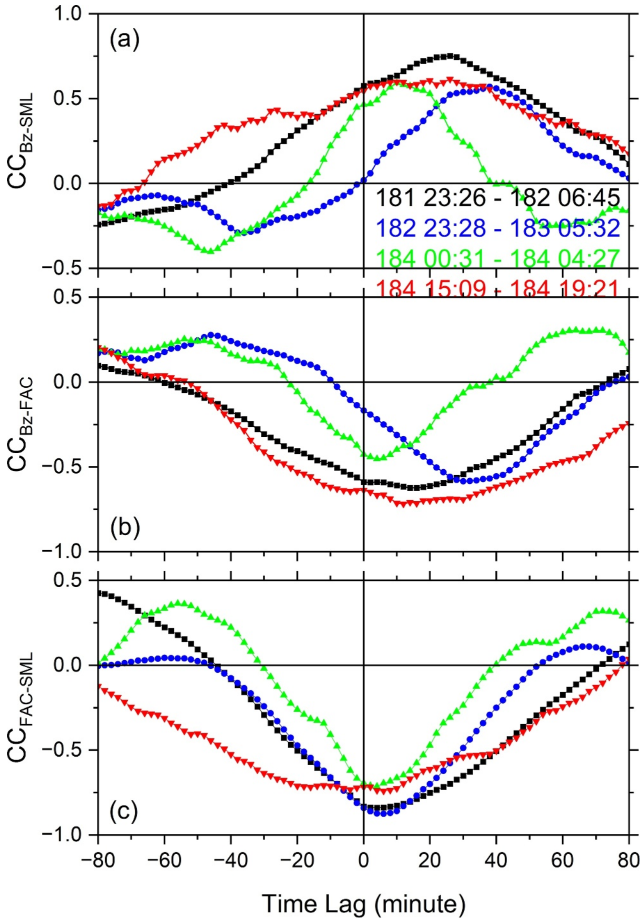

Figure 5. Cross-correlation analyses during the HILDCAA event shown in Figure 2. Time-lagged cross-correlation coefficients (CC) between (a) IMF B_z and SML, (b) B_z and upward total FAC intensity, and (c) upward total FAC intensity and SML for four intervals indicated in the top panel.

southern hemisphere, region 1 upward (downward) current is observed in the 2–11 MLT (13–23 MLT) sector, and region 2 downward (weaker upward) current is observed in the 4–10 MLT (15–1 MLT) sector.

At 2 days (Figures 3e and 3e′) and 3 days (Figures 3f and 3f′) after the HILDCAA onset, the variations of the sunlit and dark SML indices are consistent with the FAC maps.

Figure 4 shows wavelet spectrum periodograms of SML (Figure 4b) and upward total FAC intensity (Figure 4c) during the HILDCAA shown in Figure 2. The HILDCAA interval is characterized by high-power (red regions in the periodograms) SML and FAC fluctuations of varying periods (inside the cone of influence). The periodic variations of SML and FAC are more or less identical during the HILDCAA event. Besides the ∼49-hr periodicity, the major part of which may be distorted by the edge effect, the SML variation is dominated by a ∼19-hr periodicity that exhibits a quasi-continuous distribution during almost entire HILDCAA interval. The SML periodicities of ∼11 and ∼7 hr have intermittent distributions, around initial and final parts of the HILDCAA. The FAC wavelet periodogram is characterized by the most significant ∼19-hr periodicity with intermittent distribution around initial and final parts of the HILDCAA, and another ∼11-hr periodicity with a more local distribution.

During the HILDCAA event shown in Figure 2, we have arbitrarily chosen four intervals of 3.9–7.3-hr durations to study the relationship between the periodic variations in the SML index and the FAC intensity, and their causal relationships with IMF B_z (Figure 5). From time-lagged cross-correlation analyses, the SML index is found to exhibit peak correlation coefficients of 0.57–0.75 with B_z at time-lags of ∼10–38 min from B_z (Figure 5a). The peak correlation coefficient between upward total FAC intensity and B_z varies between −0.45 and −0.72 at time lags of ∼4–30 min (Figure 5b). In addition, SML exhibits the strongest correlation coefficient of −0.71 to −0.88 with the FAC intensity at time lags of ∼4–6 min (Figure 5c). However, given that the cross-correlation peaks are broad, and that the resolution of the AMPERE data is limited to a 10-min window, there may be an error in the time lags of at least 10 min. Thus, SML and FAC seem to exhibit no practical time lag between them.

During 42 HILDCAA events when suitable FAC measurements are available, we selected 122 intervals of durations of ∼3.7–28.2 hr for the cross-correlation analysis as above. The results are presented in Figure 6. Table 2 summarizes the statistical distributions of the cross-correlation coefficients and time lags for all studied intervals. From this statistical analysis, relationships among the periodic variations of IMF B_z, FAC and SML are found to vary from one HILDCAA to the other or even from one part of an HILDCAA to its other part. In general, periodic variation in the FAC intensity seems to be closely related to that in SML (with no significant time lags), and they seem to be driven by periodic variations in B_z at a lag of the order of ∼30 min.

3.2. Statistical FAC Intensity Distributions

We computed statistical FAC distributions using FAC intensity variations at every 2-min during all HILDCAAs under this study. The minimum-to-maximum FAC intensity range is first divided into 0.25-MA bins, and numbers of 2-min FAC observations are counted for each bin. They are then expressed as percentages of total observation counts. The HILDCAA-related FAC intensity distributions are compared with distributions of quiet time FAC measurements during 2-day intervals characterized by SYM-H > −50 nT and SME < 500 nT prior to the HILDCAA onsets. The HILDCAA-related and pre-HILDCAA (quiet) FAC intensity distributions are shown in Figure 7, and the statistical results are summarized in Table 3. The distributions are asymmetric Gaussian (non-

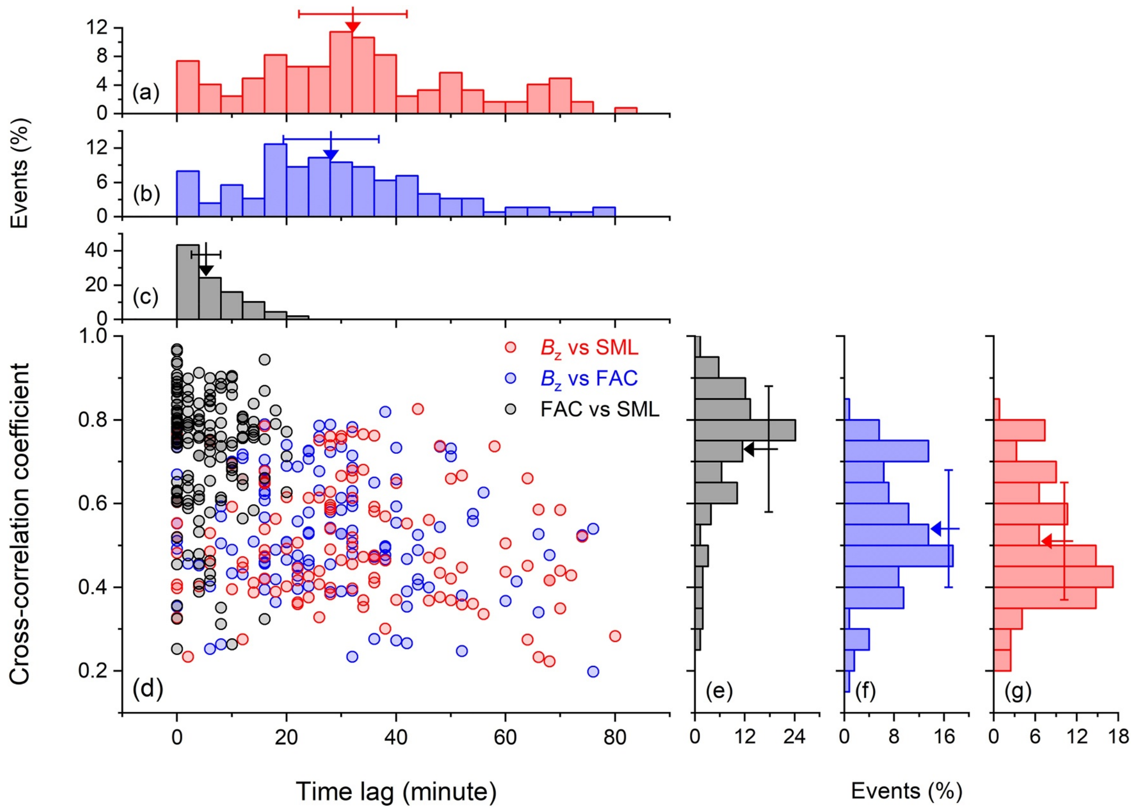

Figure 6. Statistics of cross-correlation analyses based on 122 intervals during 42 HILDCAAs under this study. Distributions of time lags of the peak cross-correlations between (a) IMF B_z and SML (red), (b) B_z and FAC intensity (blue), and (c) FAC intensity and SML (gray). (d) Variations of the peak cross-correlation coefficients with corresponding time lags between B_z and SML (red), B_z and FAC intensity (blue), and FAC intensity and SML (gray). Distributions of the peak cross-correlation coefficients between (e) FAC intensity and SML (red), (f) B_z and FAC intensity (blue), and (g) B_z and SML (gray). In panels (a–c), mean values and 1-σ deviations of the distributions are shown by downward arrows and horizontal bars, respectively, while those are shown by leftward arrows and vertical bars, respectively in panels (e–g).

normal) in nature. There are no significant differences between upward and downward current intensities (on average, differences are only ∼0%–10% during pre-HILDCAA intervals, ∼0%–3% during HILDCAAs). It can be noted from Table 3, the maximum pre-HILDCAA FAC intensity (∼21.7, 22.5 MA) is larger than during the HILDCAA events (∼19.2, 19.6 MA), implying that large FAC intensity can occur even when SME is low (<500 nT, which is the requirement for quiet time). However, the maximum FAC intensities are from single data points and may not be statistically significant.

Comparing FAC intensity distributions during HILDCAAs and pre-HILDCAA (quiet) intervals, peaks in the distributions are found to be larger for the HILDCAAs than for the pre-HILDCAA distributions, as expected (Figure 7). On average, total upward (downward) FAC intensities during HILDCAAs are ∼104% (∼108%) stronger than the pre-HILDCAA FAC intensities. However, 1-σ deviations from the mean values are significantly large. The two-tailed p-values computed for the FAC distributions during HILDCAAs and pre-HILDCAA intervals are less than 0.0001, indicating that FAC enhancements during HILDCAAs (compared to their pre-HILDCAA values) are statistically significant.

For each of the HILDCAAs, we computed a peak/maximum FAC intensity (FACp) and an average FAC intensity (<FAC>) during the event. The statistical distributions of these characteristic FACp and <FAC> values for all HILDCAAs are shown in Figure 8, and summarized in Table 4. Both FACp and <FAC> exhibit large ranges of values with no significant differences between their upward and downward components (differences are, on average, only ∼1% and ∼2%, respectively). On average, HILDCAAs are

Table 2
Statistical Mean ± 1-σ (Median) Cross-Correlation Coefficients and Time Lags Based on 122 Intervals of Durations of ∼3.7–28.2 hr During 42 HILDCAA Events

Parameters	Peak cross-correlation coefficient	Time lag (min)
B_z–SML	0.51 ± 0.14 (0.48)	32 ± 20 (30)
B_z–FAC intensity[a]	−0.54 ± 0.14 (−0.53)	28 ± 17 (26)
FAC intensity[a]–SML	−0.73 ± 0.15 (−0.76)	5 ± 5 (4)

[a]FAC intensity represents the upward total FAC intensity.

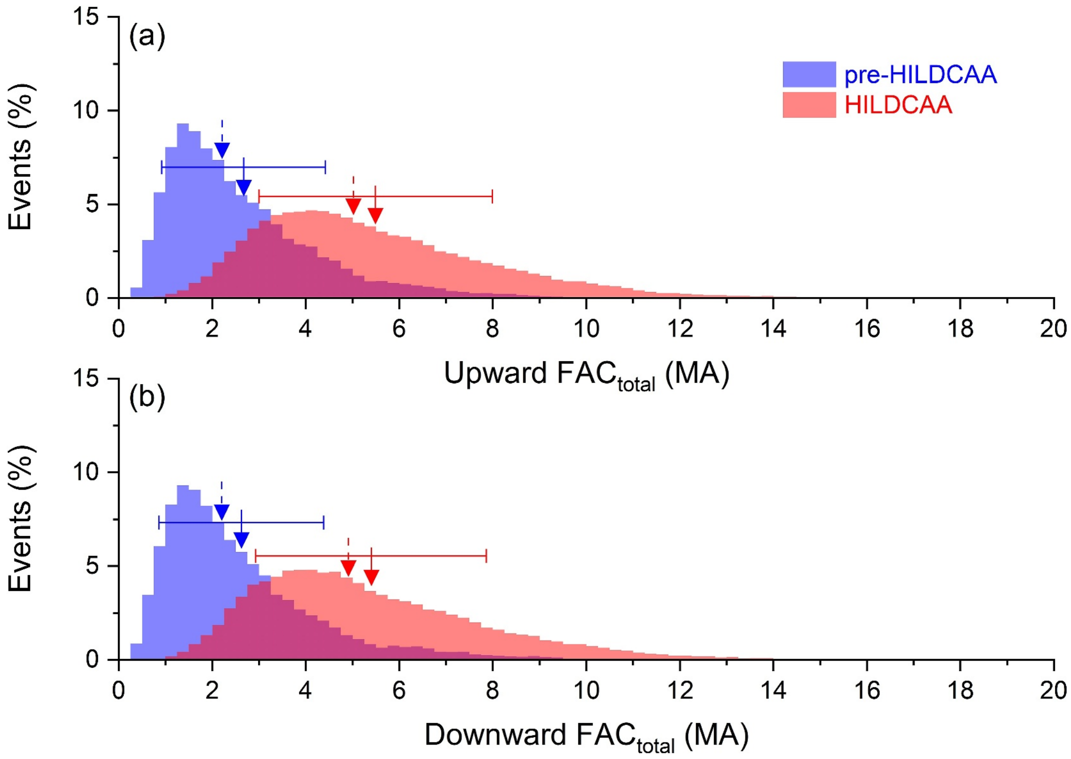

Figure 7. Distributions of (a) upward total FAC intensities and (b) downward total FAC intensities during all HILDCAAs (red) and pre-HILDCAA quiet (blue) intervals. Downward arrows indicate mean (solid) and median (dashed) values, and horizontal bars indicate 1-σ deviations of the FAC intensities for all events.

characterized by a peak and an average total (for both hemispheres) FAC intensity of ∼14 and ∼6 MA, respectively.

3.3. Superposed Epoch Analyses

Figure 9 shows superposed epoch analyses of solar wind plasma, IMF, solar wind-magnetosphere coupling functions, geomagnetic indices, and FAC intensities during all HILDCAAs. Variation of V_p indicates a typical slow stream-HSS interaction (Figure 9a). The slow and fast streams are characterized by low and high T_p (high and low plasm-β), respectively (Figure 9c). The HILDCAA onset (the zero epoch time) organizes all parameters, indicating statistical relationships among them. The onset time precedes the peaks of N_p, P_{sw} (Figure 9b), IMF B_0 (Figure 9d) by ∼2–3 hr, and coincides with a north-to-southward turning of B_z (Figure 9d). The southward IMF turning at the HILDCAA onset is followed by enhanced electric field VB_s (Figure 9e) leading to magnetic reconnection. This, in turn, leads to enhanced dayside magnetic flux transport rate Φ_D, and enhanced rate of magnetic flux opening at the magnetopause measured by N_{CF} (Figure 9f). As a result, the solar wind kinetic energy input rate ε increased significantly during the HILDCAA interval (Figure 9e). These lead to apparent geomagnetic impacts: a decreasing ring current index SYM-H (Figure 9g), enhancements in auroral activity indices SME (Figure 9h) and SML (Figure 9i), and FAC intensifications (Figure 9j). Thus, Figure 9 clearly presents the chain of processes in solar wind and magnetosphere leading to enhanced FACs during HILDCAAs.

Table 3
Statistical Features of Total FAC Intensity Distributions During Pre-HILDCAA (Quiet) Intervals and HILDCAAs

	Pre-HILDCAA total FAC intensity (MA)		HILDCAA-related total FAC intensity (MA)	
	Upward	Downward	Upward	Downward
Minimum	0.2	0.2	0.5	0.6
Maximum	21.7	22.5	19.2	19.6
Median	2.2	2.2	5.0	4.9
Mean ± 1-σ	2.7 ± 1.8	2.6 ± 1.8	5.5 ± 2.5	5.4 ± 2.5

Interestingly, the mean total FAC intensity variations show a sharp intensification at the HILDCAA onset, followed by a gradual increase (Figure 9j). FAC intensities exhibit a ∼1.8 factor increase from a pre-HILDCAA intensity of ∼3.9 to ∼6.9 MA during the HILDCAA. The FAC intensity peak occurs ∼14 hr after the HILDCAA onset. The upward and downward FACs seem to be well-correlated to the SME and SML index variations, respectively.

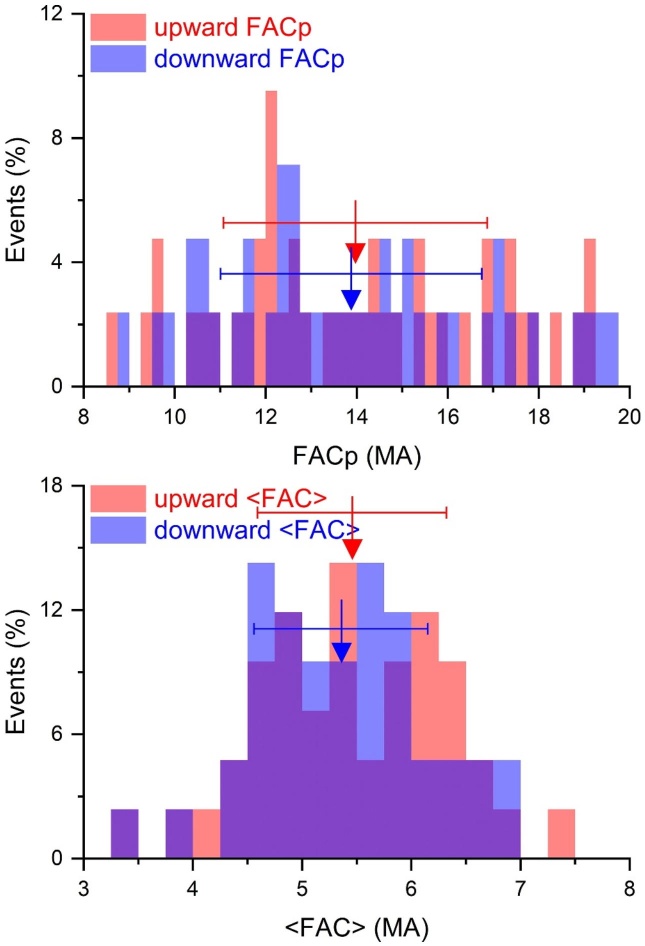

Figure 8. Distributions of (top) peak FAC intensity (FACp) and (bottom) average FAC intensity (<FAC>) during all HILDCAAs. Downward arrows and horizontal bars indicate mean intensities and 1-σ deviations, respectively, for all events. Note that different bins are used for FACp and <FAC> as their ranges are significantly different.

4. Summary and Discussions

We utilized a ∼14 years-long (October 2009 through December 2014) AMPERE database of northern and southern hemispheric FAC measurements to study statistical features of FACs during intense and long-duration global-scale convection events called HILDCAAs. Along with the FAC measurements, this study utilizes several ground-based geomagnetic indices, spacecraft observations of the near-Earth solar winds as well as observations of the sun. The major findings of this study are listed and discussed below.

1. We developed a new HILDCAA database for ∼1.5 solar cycles, which may be useful to the space community for space weather research. Higher occurrence rate of the events during the solar cycle descending-to-minimum phase, an average HILDCAA duration of ∼2.9 days, and an average peak SME intensity of ∼1,388 nT are consistent with statistical results reported by Hajra et al. (2013). The latter results, however, are based on a larger database for ∼3.5 solar cycles (1975–2011).
2. During the HILDCAAs, FAC intensities exhibit periodic variations with (statistically significant) periodicities of ∼19 and ∼11 hr (in descending order of spectral power). These are highly correlated (with a peak cross-correlation coefficient of −0.73) to similar periodic variations in the SML index. The periodic variations of FAC intensities and SML are consistent with reported periodicities in AE index during HILDCAAs (e.g., Souza et al., 2016, 2018; Tsurutani et al., 1990), attributed to interplanetary Alfvén waves (Korth et al., 2011; Tsurutani et al., 2006).
3. The HILDCAA-related SML and FAC variations exhibit plausible causative relationships with Alfvén wave IMF B_z. On average, B_z variations precede the SML variations by ∼32 ± 20 min. This is consistent with ∼20–30 min time lag reported between B_z and AE during HILDCAAs (Souza et al., 2018; Tsurutani et al., 1990). It is noted that this delay of SML/AL to IMF B_z is essentially the same for isolated substorms (Tsurutani & Meng, 1972). On the other hand, the FAC variation is found to lag the B_z variation by ∼28 ± 17 min. Coxon et al. (2014) reported that Φ_D peaks slightly before the substorm onset, while the FAC intensity maximizes in the substorm expansion phase, implying a significant time lag between solar wind-magnetosphere coupling and the FAC intensification. Pedersen et al. (2023) reported a time lag of 40 ± 10 min between total FAC intensity (SME) and N_{CF} during geomagnetic storms driven by HSSs/CIRs and sheaths, and a lag of 60 ± 10 min for magnetic cloud (MC)-driven storms. Thus, the HILDCAA-related FAC response time to solar wind parameters is much closer to that for storms driven by HSSs/CIRs and sheaths. This consistency (and discrepancy with MC-driven storms) is because HILDCAAs are associated with CIRs followed by HSSs. The short time lag between the FAC intensity and IMF B_z may indicate that FAC variations are "directly driven" by solar wind/IMF B_z (Akasofu et al., 1985; Bargatze et al., 1985).
4. Based on a statistical study of total northern and southern hemispheric FAC intensities during pre-HILDCAA (geomagnetically quiet) intervals, the average upward (downward) nominal FAC intensity during quiet times is estimated to be ∼2.7 ± 1.8 (2.6 ± 1.8) MA. The characteristic average and peak FAC intensities for the HILDCAAs are ∼5.5 ± 0.9 MA and ∼14.0 ± 2.9 MA, respectively. Thus, the average and peak FAC intensities determined during the HILDCAAs are, on average, ∼2 and ∼5 times the quiet time FAC intensities, respectively. Analysis of FAC density maps indicates a FAC intensification extending from the pole down to ∼65° magnetic latitude during a HILDCAA. These results clearly indicate generation of strong FACs during HILDCAAs, for the first time. How do the HILDCAA-related FAC variations compare with FACs during

Table 4
Characteristic FAC Intensity Statistical Parameters During HILDCAAs

	HILDCAA FACp (MA)		HILDCAA <FAC> (MA)	
	Upward	Downward	Upward	Downward
Minimum	8.7	8.8	3.3	3.3
Maximum	19.2	19.6	7.4	6.9
Median	13.7	13.4	5.5	5.4
Mean ± 1-σ	14.0 ± 2.9	13.9 ± 2.9	5.5 ± 0.9	5.4 ± 0.8

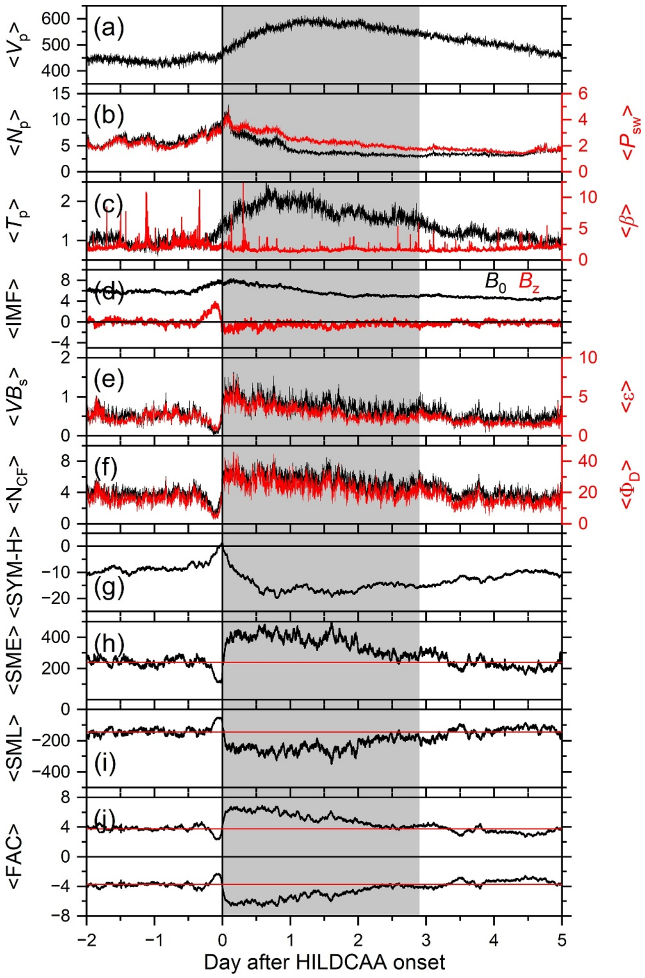

Figure 9. Superposed epoch analyses during all HILDCAAs. From top to bottom, panels are: mean temporal variations of (a) V_p (km s^{-1}), (b) N_p (cm^{-3}, black, legend on the left) and P_{sw} (nPa, red, legend on the right), (c) T_p (K, black, legend on the left) and β (red, legend on the right), (d) IMF B_0 (nT, black) and B_z (nT, red), (e) VB_s (mV m^{-1}, black, legend on the left) and ε (10^{11} W, red, legend on the right), (f) N_{CF} (10^3 Wb s^{-1}, black, legend on the left) and Φ_D (kV, red, legend on the right), (g) SYM-H (nT), (h) SME (nT), (i) SML (nT), and (j) total FAC intensities (MA). The zero epoch time (marked by a black vertical line) corresponds to the HILDCAA onset time. Mean HILDCAA duration is marked by a vertical gray shading. The red horizontal lines in panels (h–j) indicate pre-HILDCAA average levels of the parameters.

substorms and geomagnetic storms? Based on a study of FACs during 2900 substorms, Coxon et al. (2014) reported a FAC intensification in the substorm growth phase, maximizing during the expansion phase, followed by a decrease to pre-substorm levels in the recovery phase. Total increase in FAC intensity over a substorm cycle was found to be ∼1 MA, significantly lower than the FAC intensification during HILDCAAs (present work). Wang et al. (2006) reported FAC intensification during intense storms (with the Dst intensities of −180, −363, −401, and −472 nT) in October and November 2003 by a factor of 5 compared to quiet time FAC intensities. Analyses of global FAC density maps during two recent storms, April 2023 SYM-H = −233 nT storm (Hajra, Tsurutani, Lu, Horne, et al., 2024) and May 2024 SYM-H = −518 nT storm (Hajra, Tsurutani, Lakhina, et al., 2024; Wang et al., 2024), revealed FACs expanding down to ∼50° magnetic latitude (larger expansion than during HILDCAAs), and FAC intensification by a factor of ∼10 than quiet time values. The FAC intensification during a HILDCAA (present work) is, thus, ∼1/2 times the FAC intensification during extreme geomagnetic storms.

5. Superposed epoch analyses are conducted to study statistical relationships among solar wind plasma, IMF, solar wind-magnetosphere coupling functions, geomagnetic indices, and FAC intensities during HILDCAAs. The HILDCAA onset is associated with an interaction of an HSS with background slow stream leading to a CIR characterized by plasma and IMF compressions, and a southward turning of IMF. These are consistent with statistical results presented in Hajra et al. (2014a, 2014c, 2015a, 2015b) for other sets of HILDCAA events. Superposed mean FAC intensity profile is characterized by a sharp increase at the HILDCAA onset, followed by a gradual increase leading to a ∼1.8 factor FAC intensification (compared to the pre-HILDCAA FAC intensity) ∼14 hr after the HILDCAA onset. Based on statistical studies during geomagnetic storms, FAC intensities are reported to peak in the storm main phase, ∼40 min and ∼1 hr after the onset of storms driven by CIRs/HSSs (Pedersen et al., 2021) and interplanetary coronal mass ejections (ICMEs) (Pedersen et al., 2022), respectively. Evidently, present study reveals a slower and sustained development of FACs during the HILDCAAs compared to the storm-related FAC responses.
6. The HILDCAA-related FAC intensification exhibits an apparent cause-effect relationship with enhanced Φ_D, N_{CF}, ε, and VB_s. These parameters quantify magnetic reconnection and consequent magnetospheric energy flow. The superposed epoch analysis clearly suggests that during HILDCAAs, characterized by the HSS Alfvén wave southward IMFs, rate of the magnetic reconnection (Φ_D) at the dayside magnetopause increases, leading to increased generation of open magnetic fluxes (N_{CF}), and enhanced flow of solar wind kinetic energy (ε) and motional electric fields (VB_s). These, in turn, are manifested by increased FAC intensities during the HILDCAAs. These results are, in general, consistent with relationship of FACs with Φ_D during isolated substorms (e.g., Coxon et al., 2014), and with FAC–solar wind relationships during geomagnetic storms (e.g., Pedersen et al., 2021, 2022).

5. Concluding Remarks

Although considerable effort was done studying FACs during auroral substorms and geomagnetic storms, FAC behavior during HILDCAAs had not been previously examined. Why would one expect the results to be different? Substorm studies usually involve the quiet solar wind (e.g., Akasofu, 1964; Tsurutani & Meng, 1972). Magnetic storm studies typically involve ICMEs and their sheaths (e.g., Echer et al., 2008; Tsurutani et al., 1988, 1990, 1992, 2024). HILDCAAs typically involve HSSs (e.g., Hajra et al., 2013;

Tsurutani & Gonzalez, 1987). In addition, it is important to note geophysical differences among different types of geomagnetic disturbances. As discussed in Gonzalez et al. (1994), geomagnetic storms are associated with intense magnetospheric convection electric fields continuing for a few hours, bringing the ring current closer to the Earth. Substorms may be caused by modest levels of convection electric fields continuing for an hour of less. HILDCAAs, involving intense substorm/convection events continuing for days to weeks, are associated with intense and discrete convection electric fields repeating for days to weeks. Are these differences reflected in HILDCAA-related FAC variation compared to during substorms and storms? HILDCAA-related FAC intensity is significantly higher than during isolated substorms, and is sometimes comparable to during intense geomagnetic storms. During HILDCAAs, FAC distribution is expanded from near-pole region down to ~65° magnetic latitude. This is, again, significantly larger than during isolated substorms, but lower than during extreme geomagnetic storms. In addition, long intervals of HILDCAAs are associated with characteristic periodic variations in FACs, which were not reported before. We encourage more detail studies of FACs involving different natures of geomagnetic disturbances.

Appendix A: Solar Images and Synoptic Maps

Figure A1 shows evolution of NOAA coronal hole 21 emanating the HSS shown in Figure 2. From the SDO/AIA 193 Å solar images (Figures A1a–A1d), the coronal hole is found to emerge over the eastern limb of the sun on day 176 (24 June), expanded in size and turned directly toward Earth and arrived at the center of the sun on day 181 (29 June). As confirmed by the solar synoptic map analysis (Figures A1e–A1h), the coronal hole had a negative magnetic polarity (i.e., magnetic field pointing toward the sun).

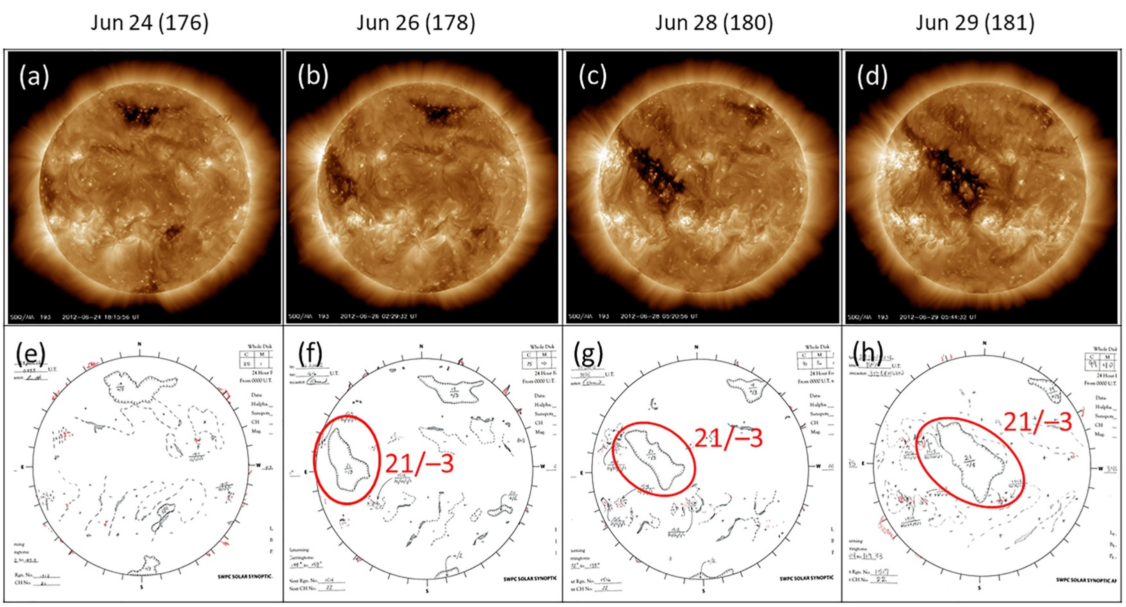

Figure A1. (a–d) SDO/AIA solar images at the wavelength of 193 Å, and (e–h) NOAA solar synoptic maps taken on 24, 26, 28, and 29 June 2012. Red ovals mark the coronal hole (NOAA) number 21, along with its polarity (−), and 3 representing a "fair" confidence level of the coronal hole analysis.

Conflict of Interest

The authors declare no conflicts of interest relevant to this study.

Data Availability Statement

The FAC data are obtained from the AMPERE Science Data Center of the Johns Hopkins Applied Physics Laboratory (https://ampere.jhuapl.edu/). The data is free to download from the download page under the AMPERE Derived Product Data Files (Daily) (https://ampere.jhuapl.edu/download/?page=derivedProductsTab).

The near-Earth solar wind plasma and IMF data are obtained from NASA's OMNIWeb Plus database (https://omniweb.gsfc.nasa.gov/). The high-resolution data can be directly downloaded from the page: https://omniweb.gsfc.nasa.gov/form/omni_min.html, by specifying start and stop times. The solar coronal images are obtained from NASA's Solar Dynamics Observatory (SDO; https://sdo.gsfc.nasa.gov/). The SDO/AIA images are freely available to view and download from the page: https://sdo.gsfc.nasa.gov/data/aiahmi/, by specific time, resolution etc. The solar synoptic maps are obtained from NOAA Space Weather Prediction Center (NOAA; www.swpc.noaa.gov/). The maps are collected from the site (https://www.ngdc.noaa.gov/stp/space-weather/solar-data/solar-imagery/composites/full-sun-drawings/boulder/) archiving year wise data. The geomagnetic Dst, AE, and SYM-H indices are obtained from the World Data Center for Geomagnetism, Kyoto, Japan (https://wdc.kugi.kyoto-u.ac.jp/). Specific index can be freely downloaded from the Data Service page (https://wdc.kugi.kyoto-u.ac.jp/wdc/Sec3.html) by selecting the index and then specifying start and end times. The SME, SMU, and SML indices are obtained from the SuperMAG database (https://supermag.jhuapl.edu/). The indices are freely available to plot and download through the Indices page (https://supermag.jhuapl.edu/indices/?fidelity=low&layers=SME.UL&start=2001-01-29T16%3A00%3A00.000Z&step=14400&tab=plot) by specifying time, duration and selecting the indices. The $F_{10.7}$ solar fluxes are obtained from the Laboratory for Atmospheric and Space Physics (LASP) Interactive Solar Irradiance Data Center (https://lasp.colorado.edu/lisird/).

Acknowledgments

The work of R. H. is funded by the "Hundred Talents Program" of the Chinese Academy of Sciences (CAS), and the "Excellent Young Scientists Fund Program (Overseas)" of the National Natural Science Foundation of China (NSFC). We would like to thank the reviewers for extremely valuable suggestions that substantially improved the manuscript.

References

Abraham-Shrauner, B. (1972). Determination of magnetohydrodynamic shock normal. *Journal of Geophysical Research*, *77*(4), 736–739. https://doi.org/10.1029/JA077i004p00736

Ahn, B.-H., Kroehl, H. W., Kamide, Y., & Kihn, E. A. (2000). Universal time variations of the auroral electrojet indices. *Journal of Geophysical Research*, *105*(A1), 267–275. https://doi.org/10.1029/1999JA900364

Akasofu, S. I. (1964). The development of the auroral substorm. *Planetary and Space Science*, *12*(4), 273–282. https://doi.org/10.1016/0032-0633(64)90151-5

Akasofu, S.-I., Olmsted, C., Smith, E. J., Tsurutani, B. T., Okida, R., & Baker, D. N. (1985). Solar wind variations and geomagnetic storms: A study of individual storms based on high time resolution ISEE 3 data. *Journal of Geophysical Research*, *90*(A1), 325–340. https://doi.org/10.1029/JA090iA01p00325

Alfvén, H. (1942). Existence of electromagnetic-hydrodynamic waves. *Nature*, *150*(3805), 405–406. https://doi.org/10.1038/150405d0

Anderson, B. J., Angappan, R., Barik, A., Vines, S. K., Stanley, S., Bernasconi, P. N., et al. (2021). Iridium communications satellite constellation data for study of Earth's magnetic field. *Geochemistry, Geophysics, Geosystems*, *22*(8), e2020GC009515. https://doi.org/10.1029/2020GC009515

Anderson, B. J., Korth, H., Waters, C. L., Green, D. L., Merkin, V. G., Barnes, R. J., & Dyrud, L. P. (2014). Development of large-scale Birkeland currents determined from the active magnetosphere and planetary electrodynamics response experiment. *Geophysical Research Letters*, *41*(9), 3017–3025. https://doi.org/10.1002/2014GL059941

Anderson, B. J., Takahashi, K., Kamei, T., Waters, C. L., & Toth, B. A. (2002). Birkeland current system key parameters derived from Iridium observations: Method and initial validation results. *Journal of Geophysical Research*, *107*(A6), SMP11-1–SMP11-13. https://doi.org/10.1029/2001JA000080

Anderson, B. J., Takahashi, K., & Toth, B. A. (2000). Sensing global Birkeland currents with iridium® engineering magnetometer data. *Geophysical Research Letters*, *27*(24), 4045–4048. https://doi.org/10.1029/2000GL000094

Axford, W. I., & Hines, C. O. (1961). A unifying theory of high-latitude geophyaical phenomena and geomagnetic storms. *Canadian Journal of Physics*, *39*(10), 1433–1464. https://doi.org/10.1139/p61-172

Baker, K., & Wing, S. (1989). A new magnetic coordinate system for conjugate studies at high latitudes. *Journal of Geophysical Research*, *94*(A7), 9139–9143. https://doi.org/10.1029/JA094iA07p09139

Bargatze, L. F., Baker, D. N., McPherron, R. L., & Hones, E. W., Jr. (1985). Magnetospheric impulse response for many levels of geomagnetic activity. *Journal of Geophysical Research*, *90*(A7), 6387–6394. https://doi.org/10.1029/JA090iA07p06387

Belcher, J. W., & Davis, L., Jr. (1971). Large-amplitude Alfvén waves in the interplanetary medium, 2. *Journal of Geophysical Research*, *76*(16), 3534–3563. https://doi.org/10.1029/JA076i016p03534

Birkeland, K. (1908). *The Norwegian aurora Polaris expedition 1902–1903* (Vol. 1). H. Aschelhoug & Co. Christiania, Norway.

Birkeland, K. (1913). *The Norwegian aurora Polaris expedition 1902–1903* (Vol. 2). H. Aschelhoug & Co. Christiania, Norway.

Burlaga, L. F. (1974). Interplanetary stream interfaces. *Journal of Geophysical Research*, *79*(25), 3717–3725. https://doi.org/10.1029/JA079i025p03717

Burton, R. K., McPherron, R. L., & Russell, C. T. (1975). An empirical relationship between interplanetary conditions and Dst. *Journal of Geophysical Research*, *80*(31), 4204–4214. https://doi.org/10.1029/JA080i031p04204

Chapman, S., & Ferraro, V. C. A. (1931). A new theory of magnetic storms, part I, The initial phase. *Terrestrial Magnetism and Atmospheric Electricity*, *36*(2), 77–97. https://doi.org/10.1029/TE036i002p00077

Cheng, Z. W., Shi, J. K., Zhang, J. C., Torkar, K., Kistler, L. M., Dunlop, M., et al. (2018). Influence of the IMF cone angle on invariant latitudes of polar region footprints of FACs in the magnetotail: Cluster observation. *Journal of Geophysical Research: Space Physics*, *123*(4), 2588–2597. https://doi.org/10.1002/2017JA024941

Clausen, L. B. N., Baker, J. B. H., Ruohoniemi, J. M., Milan, S. E., & Anderson, B. J. (2012). Dynamics of the region 1 Birkeland current oval derived from the active magnetosphere and planetary electrodynamics response experiment (AMPERE). *Journal of Geophysical Research*, *117*(A6), A06233. https://doi.org/10.1029/2012JA017666

Coleman, P. J. (1966). Hydromagnetic waves in the interplanetary plasma. *Physical Review Letters*, *17*(4), 207–211. https://doi.org/10.1103/PhysRevLett.17.207

Cowley, S. W. H. (2000). Magnetosphere-ionosphere interactions: A tutorial review. In S.-I. Ohtani, R. Fujii, M. Hesse, & R. L. Lysak (Eds.), *Magnetospheric current systems*. https://doi.org/10.1029/GM118p0091

Coxon, J. C., Milan, S. E., Carter, J. A., Clausen, L. B. N., Anderson, B. J., & Korth, H. (2016). Seasonal and diurnal variations in AMPERE observations of the Birkeland currents compared to modeled results. *Journal of Geophysical Research: Space Physics*, *121*(5), 4027–4040. https://doi.org/10.1002/2015JA022050

Coxon, J. C., Milan, S. E., Clausen, L. B. N., Anderson, B. J., & Korth, H. (2014). A superposed epoch analysis of the regions 1 and 2 Birkeland currents observed by AMPERE during substorms. *Journal of Geophysical Research: Space Physics*, *119*(12), 9834–9846. https://doi.org/10.1002/2014JA020500

Davis, J. C. (2002). *Statistics and data analysis in geology* (3rd ed.). Wiley.

Dungey, J. W. (1961). Interplanetary magnetic field and the auroral zones. *Physical Review Letters*, *6*(2), 47–48. https://doi.org/10.1103/PhysRevLett.6.47

Echer, E., Gonzalez, W. D., Tsurutani, B. T., & Gonzalez, A. L. C. (2008). Interplanetary conditions causing intense geomagnetic storms (Dst ≤ −100 nT) during solar cycle 23 (1996–2006). *Journal of Geophysical Research*, *113*(A5), A05221. https://doi.org/10.1029/2007JA012744

Finch, I. D., Lockwood, M. L., & Rouillard, A. P. (2008). Effects of solar wind magnetosphere coupling recorded at different geomagnetic latitudes: Separation of directly-driven and storage/release systems. *Geophysical Research Letters*, *35*(21), L21105. https://doi.org/10.1029/2008GL035399

Forsyth, C., Shortt, M., Coxon, J. C., Rae, I. J., Freeman, M. P., Kalmoni, N. M. E., et al. (2018). Seasonal and temporal variations of field-aligned currents and ground magnetic deflections during substorms. *Journal of Geophysical Research: Space Physics*, *123*(4), 2696–2713. https://doi.org/10.1002/2017JA025136

Fujii, R., Iijima, T., Potemra, T. A., & Sugiura, M. (1981). Seasonal dependence of large-scale Birkeland currents. *Geophysical Research Letters*, *8*(10), 1103–1106. https://doi.org/10.1029/GL008i010p01103

Gibbons, J. D., & Chakraborti, S. (2011). Nonparametric statistical inference. In M. Lovric (Ed.), *International encyclopedia of statistical science* (pp. 977–979). Springer. Berlin, Heidelberg. https://doi.org/10.1007/978-3-642-04898-2_420

Gjerloev, J. (2009). A global ground-based magnetometer initiative. *Eos, Transactions American Geophysical Union*, *90*(27), 230–231. https://doi.org/10.1029/2009EO270002

Gjerloev, J. (2012). The SuperMAG data processing technique. *Journal of Geophysical Research*, *117*(A9), A09213. https://doi.org/10.1029/2012JA017683

Gonzalez, W. D., Joselyn, J. A., Kamide, Y., Kroehl, H. W., Rostoker, G., Tsurutani, B. T., & Vasyliunas, V. M. (1994). What is a geomagnetic storm? *Journal of Geophysical Research*, *99*(A4), 5771–5792. https://doi.org/10.1029/93JA02867

Gosling, J., Asbridge, J., Bame, S., & Feldman, W. (1978). Solar wind stream interfaces. *Journal of Geophysical Research*, *83*(A4), 1401–1412. https://doi.org/10.1029/JA083iA04p01401

Guarnieri, F. L., Tsurutani, B. T., Vieira, L. E. A., Hajra, R., Echer, E., Mannucci, A. J., & Gonzalez, W. D. (2018). A correlation study regarding the AE index and ACE solar wind data for Alfvénic intervals using wavelet decomposition and reconstruction. *Nonlinear Processes in Geophysics*, *25*(1), 67–76. https://doi.org/10.5194/npg-25-67-2018

Hajra, R. (2021a). Variation of the interplanetary shocks in the inner heliosphere. *The Astrophysical Journal*, *917*(2), 91. https://doi.org/10.3847/1538-4357/ac0897

Hajra, R. (2021b). September 2017 space-weather events: A study on magnetic reconnection and geoeffectiveness. *Solar Physics*, *296*(3), 50. https://doi.org/10.1007/s11207-021-01803-7

Hajra, R., Echer, E., Franco, A. M. S., & Bolzan, M. J. A. (2023). Earth's magnetotail variability during supersubstorms (SSSs): A study on solar wind–magnetosphere–ionosphere coupling. *Advances in Space Research*, *72*(4), 1208–1223. https://doi.org/10.1016/j.asr.2023.04.013

Hajra, R., Echer, E., Tsurutani, B. T., & Gonzalez, W. D. (2013). Solar cycle dependence of high-intensity long-duration continuous AE activity (HILDCAA) events, relativistic electron predictors? *Journal of Geophysical Research: Space Physics*, *118*(9), 5626–5638. https://doi.org/10.1002/jgra.50530

Hajra, R., Echer, E., Tsurutani, B. T., & Gonzalez, W. D. (2014a). Superposed epoch analyses of HILDCAAs and their interplanetary drivers: Solar cycle and seasonal dependences. *Journal of Atmospheric and Solar-Terrestrial Physics*, *121*(A), 24–31. https://doi.org/10.1016/j.jastp.2014.09.012

Hajra, R., Echer, E., Tsurutani, B. T., & Gonzalez, W. D. (2014b). Solar wind-magnetosphere energy coupling efficiency and partitioning: HILDCAAs and preceding CIR storms during solar cycle 23. *Journal of Geophysical Research: Space Physics*, *119*(4), 2675–2690. https://doi.org/10.1002/2013JA019646

Hajra, R., Franco, A. M. S., Echer, E., & Bolzan, M. J. A. (2021). Long-term variations of the geomagnetic activity: A comparison between the strong and weak solar activity cycles and implications for the space climate. *Journal of Geophysical Research: Space Physics*, *126*(4), e2020JA028695. https://doi.org/10.1029/2020JA028695

Hajra, R., Henri, P., Myllys, M., Héritier, K. L., Galand, M., Simon Wedlund, C., et al. (2018). Cometary plasma response to interplanetary corotating interaction regions during 2016 June–September: A quantitative study by the Rosetta Plasma Consortium. *Monthly Notices of the Royal Astronomical Society*, *480*(4), 4544–4556. https://doi.org/10.1093/mnras/sty2166

Hajra, R., & Tsurutani, B. T. (2018). Interplanetary shocks inducing magnetospheric supersubstorms (SML < −2500 nT): Unusual auroral morphologies and energy flow. *The Astrophysical Journal*, *858*(2), 123. https://doi.org/10.3847/1538-4357/aabaed

Hajra, R., Tsurutani, B. T., Echer, E., & Gonzalez, W. D. (2014c). Relativistic electron acceleration during high-intensity, long-duration, continuous AE activity (HILDCAA) events: Solar cycle phase dependences. *Geophysical Research Letters*, *41*(6), 1876–1881. https://doi.org/10.1002/2014GL059383

Hajra, R., Tsurutani, B. T., Echer, E., Gonzalez, W. D., Brum, C. G. M., Vieira, L. E. A., & Santolik, O. (2015a). Relativistic electron acceleration during HILDCAA events: Are precursor CIR magnetic storms important? *Earth Planets and Space*, *67*(1), 109. https://doi.org/10.1186/s40623-015-0280-5

Hajra, R., Tsurutani, B. T., Echer, E., Gonzalez, W. D., & Gjerloev, J. W. (2016). Supersubstorms (SML < −2500 nT): Magnetic storm and solar cycle dependences. *Journal of Geophysical Research: Space Physics*, *121*(8), 7805–7816. https://doi.org/10.1002/2015JA021835

Hajra, R., Tsurutani, B. T., Echer, E., Gonzalez, W. D., & Santolik, O. (2015b). Relativistic ($E > 0.6$, > 2.0, and > 4.0 MeV) electron acceleration at geosynchronous orbit during high-intensity, long-duration, continuous AE activity (HILDCAA) events. *The Astrophysical Journal*, *799*(1), 39. https://doi.org/10.1088/0004-637X/799/1/39

Hajra, R., Tsurutani, B. T., & Lakhina, G. S. (2020). The complex space weather events of 2017 September. *The Astrophysical Journal*, *899*(1), 3. https://doi.org/10.3847/1538-4357/aba2c5

Hajra, R., Tsurutani, B. T., Lakhina, G. S., Lu, Q., & Du, A. (2024). Interplanetary causes and impacts of the 2024 May superstorm on the geosphere: An overview. *The Astrophysical Journal*, *974*(2), 264. https://doi.org/10.3847/1538-4357/ad7462

Hajra, R., Tsurutani, B. T., Lakhina, G. S., Lu, Q., Du, A., & Shan, L. (2023). Interplanetary Shocks between 0.3 and 1.0 au: Helios 1 and 2 observations. *The Astrophysical Journal*, *951*, 75. https://doi.org/10.3847/1538-4357/acd370

Hajra, R., Tsurutani, B. T., Lu, Q., Du, A., Lu, S., & Echer, E. (2025). Solar cycle and seasonal dependences of field-aligned currents. *Space Weather*, *23*(5), e2025SW004441. https://doi.org/10.1029/2025SW004441

Hajra, R., Tsurutani, B. T., Lu, Q., Horne, R. B., Lakhina, G. S., Yang, X., et al. (2024). The April 2023 SYM-H = −233 nT geomagnetic storm: A classical event. *Journal of Geophysical Research: Space Physics*, *129*(10), e2024JA032986. https://doi.org/10.1029/2024JA032986

Hajra, R., Tsurutani, B. T., Lu, Q., Lakhina, G. S., Du, A., Echer, E., et al. (2024). Ultra-relativistic electron acceleration during high-intensity long-duration continuous auroral electrojet activity events. *The Astrophysical Journal*, *965*(2), 146. https://doi.org/10.3847/1538-4357/ad2dfe

Hugoniot, H. (1887). Mémoire sur la propagation des mouvements dans les corps et spécialement dans les gaz parfaits (première partie). *Journal de l'École Polytechnique*, *57*, 3–97.

Hugoniot, H. (1889). Mémoire sur la propagation des mouvements dans les corps et spécialement dans les gaz parfaits (deuxième partie). *Journal de l'École Polytechnique*, *58*, 1–125.

Hundhausen, A. J., & Burlaga, L. F. (1975). A model for the origin of solar wind stream interfaces. *Journal of Geophysical Research*, *80*(13), 1845–1848. https://doi.org/10.1029/JA080i013p01845

Iijima, T., & Potemra, T. A. (1976). Field-aligned currents in the dayside cusp observed by Triad. *Journal of Geophysical Research*, *81*(34), 5971–5979. https://doi.org/10.1029/JA081i034p05971

Iijima, T., & Potemra, T. A. (1978). Large-scale characteristics of field-aligned currents associated with substorms. *Journal of Geophysical Research*, *83*(A2), 599–615. https://doi.org/10.1029/JA083iA02p00599

Käki, S., Viljanen, A., Juusola, L., & Kauristie, K. (2022). Spatio-temporal development of large-scale auroral electrojet currents relative to substorm onsets. *Annales Geophysicae*, *40*(1), 107–119. https://doi.org/10.5194/angeo-40-107-2022

Kamide, Y., & Akasofu, S.-I. (1983). Notes on the auroral electrojet indices. *Reviews of Geophysics*, *21*(7), 1647–1656. https://doi.org/10.1029/RG021i007p01647

King, J. H., & Papitashvili, N. E. (2020). OMNI 1-min data set [Dataset]. *NASA Space Physics Data Facility*. https://doi.org/10.48322/45BB-8792

Knipp, D. J., Matsuo, T., Kilcommons, L., Richmond, A., Anderson, B., Korth, H., et al. (2014). Comparison of magnetic perturbation data from LEO satellite constellations: Statistics of DMSP and AMPERE. *Space Weather*, *12*(1), 2–23. https://doi.org/10.1002/2013SW000987

Korth, A., Echer, E., Zong, Q.-G., Guarnieri, F. L., Fraenz, M., & Mouikis, C. G. (2011). The response of the polar cusp to a high-speed solar wind stream studied by a multispacecraft wavelet analysis. *Journal of Atmospheric and Solar-Terrestrial Physics*, *73*(1), 52–60. https://doi.org/10.1016/j.jastp.2009.10.004

Kozyra, J. U., Crowley, G., Emery, B. A., Fang, X., Maris, G., Mlynczak, M. G., et al. (2006). Response of the upper/middle atmosphere to coronal holes and powerful high-speed solar wind streams in 2003. In B. Tsurutani, R. McPherron, G. Lu, J. H. A. Sobral, & N. Gopalswamy (Eds.), *Recurrent magnetic storms: Corotating solar wind streams*. https://doi.org/10.1029/167GM24

Krieger, A., Timothy, A., & Roelof, E. (1973). A coronal hole and its identification as the source of a high velocity solar wind stream. *Solar Physics*, *29*(2), 505–525. https://doi.org/10.1007/BF00150828

Laundal, K. M., Finlay, C. C., Olsen, N., & Reistad, J. P. (2018). Solar wind and seasonal influence on ionospheric currents from Swarm and CHAMP measurements. *Journal of Geophysical Research: Space Physics*, *123*(5), 4402–4429. https://doi.org/10.1029/2018JA025387

Le, G., Lühr, H., Anderson, B. J., Strangeway, R. J., Russell, C. T., Singer, H., et al. (2016). Magnetopause erosion during the 17 March 2015 magnetic storm: Combined field-aligned currents, auroral oval, and magnetopause observations. *Geophysical Research Letters*, *43*(6), 2396–2404. https://doi.org/10.1002/2016GL068257

Lyons, L. R., Gallardo-Lacourt, B., Zou, S., Weygand, J. M., Nishimura, Y., Li, W., et al. (2016). The 17 March 2013 storm: Synergy of observations related to electric field modes and their ionospheric and magnetospheric effects. *Journal of Geophysical Research: Space Physics*, *121*(11), 10880–10897. https://doi.org/10.1002/2016JA023237

Mendes, O., Domingues, M. O., Echer, E., Hajra, R., & Menconi, V. E. (2017). Characterization of high-intensity, long-duration continuous auroral activity (HILDCAA) events using recurrence quantification analysis. *Nonlinear Processes in Geophysics*, *24*(3), 407–417. https://doi.org/10.5194/npg-24-407-2017

Milan, S., Gosling, J., & Hubert, B. (2012). Relationship between interplanetary parameters and the magnetopause reconnection rate quantified from observations of the expanding polar cap. *Journal of Geophysical Research*, *117*(A3), A03226. https://doi.org/10.1029/2011JA017082

Neugebauer, M., Clay, D. R., Goldstein, B. E., Tsurutani, B. T., & Zwickl, R. D. (1984). A reexamination of rotational and tangential discontinuities in the solar wind. *Journal of Geophysical Research*, *89*(A7), 5395–5408. https://doi.org/10.1029/JA089iA07p05395

Neugebauer, M., & Snyder, C. W. (1966). Mariner 2 observations of the solar wind: 1. Average properties. *Journal of Geophysical Research*, *71*(19), 4469–4484. https://doi.org/10.1029/JZ071i019p04469

Newell, P., & Gjerloev, J. (2011a). Evaluation of SuperMAG auroral electrojet indices as indicators of substorms and auroral power. *Journal of Geophysical Research*, *116*(A12), A12211. https://doi.org/10.1029/2011JA016779

Newell, P., & Gjerloev, J. (2011b). Substorm and magnetosphere characteristic scales inferred from the SuperMAG auroral electrojet indices. *Journal of Geophysical Research*, *116*(A12), A12232. https://doi.org/10.1029/2011JA016936

Newell, P. T., Sotirelis, T., Liou, K., Meng, C. I., & Rich, F. J. (2007). A nearly universal solar wind-magnetosphere coupling function inferred from 10 magnetospheric state variables. *Journal of Geophysical Research*, *112*(A1), A01206. https://doi.org/10.1029/2006JA012015

Pedersen, M. N., Vanhamäki, H., & Aikio, A. T. (2023). Comparison of field-aligned current responses to HSS/SIR, sheath, and magnetic cloud driven geomagnetic storms. *Geophysical Research Letters*, *50*(11), e2023GL103151. https://doi.org/10.1029/2023GL103151

Pedersen, M. N., Vanhamäki, H., Aikio, A. T., Käki, S., Workayehu, A. B., Waters, C. L., & Gjerloev, J. W. (2021). Field-aligned and ionospheric currents by AMPERE and SuperMAG during HSS/SIR-driven storms. *Journal of Geophysical Research: Space Physics*, *126*(11), e2021JA029437. https://doi.org/10.1029/2021JA029437

Pedersen, M. N., Vanhamäki, H., Aikio, A. T., Waters, C. L., Gjerloev, J. W., Käki, S., & Workayehu, A. B. (2022). Effect of ICME-driven storms on field-aligned and ionospheric currents from AMPERE and SuperMAG. *Journal of Geophysical Research: Space Physics*, *127*(8), e2022JA030423. https://doi.org/10.1029/2022JA030423

Perreault, P., & Akasofu, S.-I. (1978). A study of geomagnetic storms. *Geophysical Journal International*, *54*(3), 547–573. https://doi.org/10.1111/j.1365-246X.1978.tb05494.x

Phillips, J. L., Bame, S. J., Feldman, W. C., Gosling, J. T., Hammond, C. M., McComas, D. J., et al. (1995). Ulysses solar wind plasma observations at high southerly latitudes. *Science*, *268*(5213), 1030–1033. https://doi.org/10.1126/science.268.5213.1030

Press, W. H., Teukolsky, S. A., Vetterling, W. T., & Flannery, B. P. (1992). *Numerical recipes: The art of scientific computing* (2nd ed.). Cambridge University Press. New York.

Qu, B. H., Lu, J. Y., Wang, Z. W., Liu, J. J., Wang, M., Li, J. Y., & Zhang, H. (2024). Estimation of ionospheric field-aligned currents using SuperDARN radar and DMSP observations. *Journal of Geophysical Research: Space Physics*, *129*(6), e2024JA032708. https://doi.org/10.1029/2024ja032708

Rankine, W. J. M. (1870). XV. On the thermodynamic theory of waves of finite longitudinal disturbance. *Philosophical Transactions of the Royal Society*, *160*, 277–288. https://doi.org/10.1098/rstl.1870.0015

Reiff, P. H. (1990). The use and misuse of statistics in space physics. *Journal of Geomagnetism and Geoelectricity*, *42*(9), 1145–1174. https://doi.org/10.5636/jgg.42.1145

Rostoker, G. (1972). Geomagnetic indices. *Reviews of Geophysics*, *10*(4), 935–950. https://doi.org/10.1029/RG010i004p00935

Sandanger, M. I., Søraas, F., Aarsnes, K., Oksavik, K., Evans, D. S., & Greer, M. S. (2005). Proton injections into the ring current associated with Bz variations during HILDCAA events. In T. I. Pulkkinen, N. A. Tsyganenko, & R. H. W. Friedel (Eds.), *The inner magnetosphere: Physics and modeling*. https://doi.org/10.1029/155GM26

Smith, E. J. (1985). Interplanetary shock phenomena beyond 1 AU. In B. T. Tsurutani & R. G. Stone (Eds.), *Collisionless shocks in the heliosphere: Reviews of current research*. https://doi.org/10.1029/GM035p0069

Smith, E. J., & Wolfe, J. H. (1976). Observations of interaction regions and corotating shocks between one and five AU: Pioneers 10 and 11. *Geophysical Research Letters*, *3*(3), 137–140. https://doi.org/10.1029/GL003i003p00137

Søraas, F., Aarsnes, K., Oksavik, K., Sandanger, M. I., Evans, D. S., & Greer, M. S. (2004). Evidence for particle injection as the cause of Dst reduction during HILDCAA events. *Journal of Atmospheric and Solar-Terrestrial Physics*, *66*(2), 177–186. https://doi.org/10.1016/j.jastp.2003.05.001

Souza, A. M., Echer, E., Bolzan, M. J. A., & Hajra, R. (2016). A study on the main periodicities in interplanetary magnetic field Bz component and geomagnetic AE index during HILDCAA events using wavelet analysis. *Journal of Atmospheric and Solar-Terrestrial Physics*, *149*, 81–86. https://doi.org/10.1016/j.jastp.2016.09.006

Souza, A. M., Echer, E., Bolzan, M. J. A., & Hajra, R. (2018). Cross-correlation and cross-wavelet analyses of the solar wind IMF Bz and auroral electrojet index AE coupling during HILDCAAs. *Annales Geophysicae*, *36*(1), 205–211. https://doi.org/10.5194/angeo-36-205-2018

Torrence, C., & Compo, G. P. (1998). A practical guide to wavelet analysis. *Bulletin of the American Meteorological Society*, *79*(1), 61–78. https://doi.org/10.1175/1520-0477(1998)079<0061:APGTWA>2.0.CO;2

Tsurutani, B. T., Goldstein, B. E., Smith, E. J., Gonzalez, W. D., Tang, F., Akasofu, S. I., & Anderson, R. R. (1990). The interplanetary and solar causes of geomagnetic activity. *Planetary and Space Science*, *38*(1), 109–126. https://doi.org/10.1016/0032-0633(90)90010-N

Tsurutani, B. T., & Gonzalez, W. D. (1987). The cause of high-intensity long-duration continuous AE activity (HILDCAAs): Interplanetary Alfvén wave trains. *Planetary and Space Science*, *35*(4), 405–412. https://doi.org/10.1016/0032-0633(87)90097-3

Tsurutani, B. T., Gonzalez, W. D., Gonzalez, A. L. C., Guarnieri, F. L., Gopalswamy, N., Grande, M., et al. (2006). Corotating solar wind streams and recurrent geomagnetic activity: A review. *Journal of Geophysical Research*, *111*(A7), A07S01. https://doi.org/10.1029/2005JA011273

Tsurutani, B. T., Gonzalez, W. D., Gonzalez, A. L. C., Tang, F., Arballo, J. K., & Okada, M. (1995). Interplanetary origin of geomagnetic activity in the declining phase of the solar cycle. *Journal of Geophysical Research*, *100*(A11), 21717–21733. https://doi.org/10.1029/95JA01476

Tsurutani, B. T., Gonzalez, W. D., Guarnieri, F. L., Kamide, Y., Zhou, X., & Arballo, J. K. (2004). Are high-intensity long-duration continuous AE activity (HILDCAA) events substorm expansion events? *Journal of Atmospheric and Solar-Terrestrial Physics*, *66*(2), 167–176. https://doi.org/10.1016/j.jastp.2003.08.015

Tsurutani, B. T., Gonzalez, W. D., Tang, F., Akasofu, S. I., & Smith, E. J. (1988). Origin of interplanetary southward magnetic fields responsible for major magnetic storms near solar maximum (1978–1979). *Journal of Geophysical Research*, *93*(A8), 8519–8531. https://doi.org/10.1029/JA093iA08p08519

Tsurutani, B. T., Gonzalez, W. D., Tang, F., & Lee, Y. T. (1992). Great magnetic storms. *Geophysical Research Letters*, *19*(1), 73–76. https://doi.org/10.1029/91GL02783

Tsurutani, B. T., & Hajra, R. (2023). Energetics of shock-triggered supersubstorms (SML < -2500 nT). *The Astrophysical Journal*, *946*(1), 17. https://doi.org/10.3847/1538-4357/acb143

Tsurutani, B. T., Hajra, R., Echer, E., & Gjerloev, J. W. (2015). Extremely intense (SML $\leq$–2500 nT) substorms: Isolated events that are externally triggered? *Annales Geophysicae*, *33*(5), 519–524. https://doi.org/10.5194/angeo-33-519-2015

Tsurutani, B. T., Lakhina, G. S., Pickett, J. S., Guarnieri, F. L., Lin, N., & Goldstein, B. E. (2005). Nonlinear Alfvén waves, discontinuities, proton perpendicular acceleration, and magnetic holes/decreases in interplanetary space and the magnetosphere: Intermediate shocks? *Nonlinear Processes in Geophysics*, *12*(3), 321–336. https://doi.org/10.5194/npg-12-321-2005

Tsurutani, B. T., Lakhina, G. S., Verkhoglyadova, O. P., Gonzalez, W. D., Echer, E., & Guarnieri, F. L. (2011). A review of interplanetary discontinuities and their geomagnetic effects. *Journal of Atmospheric and Solar-Terrestrial Physics*, *73*(1), 5–19. https://doi.org/10.1016/j.jastp.2010.04.001

Tsurutani, B. T., & Lin, R. P. (1985). Acceleration of >47 keV Ions and >2 keV electrons by interplanetary shocks at 1 AU. *Journal of Geophysical Research*, *90*(A1), 1–11. https://doi.org/10.1029/JA090iA01p00001

Tsurutani, B. T., & Meng, C.-I. (1972). Interplanetary magnetic-field variations and substorm activity. *Journal of Geophysical Research*, *77*(16), 2964–2970. https://doi.org/10.1029/JA077i016p02964

Tsurutani, B. T., Sen, A., Hajra, R., Lakhina, G. S., Horne, R. B., & Hada, T. (2024). Review of the August 1972 and March 1989 (Allen) space weather events: Can we learn anything new from them? *Journal of Geophysical Research: Space Physics*, *129*(7), e2024JA032622. https://doi.org/10.1029/2024JA032622

Turner, N. E., Mitchell, E. J., Knipp, D. J., & Emery, B. A. (2006). Energetics of magnetic storms driven by corotating interaction regions: A study of geoeffectiveness. In B. T. Tsurutani, R. McPherron, G. Lu, J. H. A. Sobral, & N. Gopalswamy (Eds.), *Recurrent magnetic storms: Corotating solar wind streams*. https://doi.org/10.1029/167GM11

Wang, H., Cheng, Q., Lühr, H., Zhong, Y., Zhang, K., & Xia, H. (2024). Local time and hemispheric asymmetries of field-aligned currents and polar electrojet during May 2024 superstorm periods. *Journal of Geophysical Research: Space Physics*, *129*(11), e2024JA033020. https://doi.org/10.1029/2024JA033020

Wang, H., & Lühr, H. (2023). Magnetic longitudinal and local time variations of polar electrojet and field-aligned currents. *Journal of Geophysical Research: Space Physics*, *128*(10), e2023JA031874. https://doi.org/10.1029/2023JA031874

Wang, H., Lühr, H., Ma, S. Y., Weygand, J., Skoug, R. M., & Yin, F. (2006). Field-aligned currents observed by CHAMP during the intense 2003 geomagnetic storm events. *Annales Geophysicae*, *24*(1), 311–324. https://doi.org/10.5194/angeo-24-311-2006

Waters, C. L., Anderson, B. J., Green, D. L., Korth, H., Barnes, R. J., & Vanhamäki, H. (2020). Science data products for AMPERE. In M. Dunlop & H. Lühr (Eds.), *Ionospheric multi-spacecraft analysis tools*, *ISSI scientific report series* (Vol. 17, pp. 141–165). Springer. Cham. https://doi.org/10.1007/978-3-030-26732-2_7

Waters, C. L., Anderson, B. J., & Liou, K. (2001). Estimation of global field aligned currents using the iridium® System magnetometer data. *Geophysical Research Letters*, *28*(11), 2165–2168. https://doi.org/10.1029/2000GL012725

10.1029/2025SW004353

Wilder, F. D., Crowley, G., Anderson, B. J., & Richmond, A. D. (2012). Intense dayside Joule heating during the 5 April 2010 geomagnetic storm recovery phase observed by AMIE and AMPERE. *Journal of Geophysical Research*, *117*(A5), A05207. https://doi.org/10.1029/2011JA017262

Zmuda, A. J., Martin, J. H., & Heuring, F. T. (1966). Transverse magnetic disturbances at 1100 kilometers in the auroral region. *Journal of Geophysical Research*, *71*(21), 5033–5045. https://doi.org/10.1029/JZ071i021p05033